Materials Science in Semiconductor Processing 172 (2024) 108048

Contents lists available at ScienceDirect

Materials Science in Semiconductor Processing

journal homepage: www.elsevier.com/locate/mssp

A DFT insight into optoelectronics and transport phenomena in the monoclinic $BiGaIn_2S_6$ compound for applications in renewable energy

T. Ghellab [a,b], Z. Charifi [a,b,*], H. Baaziz [a,b,**]

[a] Department of Physics, Faculty of Science, University of M'sila, 28000, M'sila, Algeria
[b] Laboratory of Physics and Chemistry of Materials, University of M'sila, Algeria

ARTICLE INFO

Keywords:
Optoelectronic
Transport phenomena
Improving *ZT*

ABSTRACT

The present study utilizes first-principles calculations grounded in density-functional theory (DFT) to examine the thermoelectric, electronic, elastic, optical, and structural properties of $BiGaIn_2S_6$. It is demonstrated that the approximated structural parameters (a, b, c, β, c/a, b/a), as well as atomic sites, correspond to the experimental data. Based on the measured elastic properties, it can be concluded that the investigated material possesses anisotropy and ductility. The computation of the electronic properties of our compound unveiled its semiconducting characteristics. The mBJ-LDA method was employed to ascertain that the compound exhibits an indirect band gap (Γ→Γ-E) of 2.711 eV. Based on the computational outcomes, it can be concluded that the real part of dielectric complex and refractive index exhibit a degree of anisotropy. The compound exhibits promising potential for optoelectronic applications due to its tolerable values of optical properties such as optical conductivity, absorption aspect, refractive index, and reflectivity. The positive Seebeck coefficient obtained from the calculation indicates that this compound can be classified as a *p*-type material. The semiconductor $BiGaIn_2S_6$ exhibits a maximum ZT value of 0.98741 when the charge carrier concentration is increased to $n = 0.14494 \times 10^{22}$ cm^{-3} or when the chemical potential lowers to 0.47499 Ryd. The material being studied demonstrates potential uses in the fields of thermoelectric and optoelectronic devices.

1. Introduction

There has been a significant increase in the need for energy in recent years, leading to heightened efforts in the pursuit of alternative energy sources that are independent of fossil fuels or traditional methods. The use of renewable energy sources has led to a shift in global attention [1,2]. The conversion of thermal and electrical resources into useable energy through the process of thermoelectricity is a captivating approach for the production of renewable energy and the effective utilization of waste heat, as supported by previous scholarly works [3–5]. The assessment of the effectiveness of thermoelectric (TE) materials is conducted through the utilization of the figure of merit (ZT). The calculation is performed utilizing the formula $ZT = \frac{\sigma S^2 T}{k_L + k_e}$, in which S denotes the Seebeck coefficient, σ represents the electrical conductivity, T signifies the absolute temperature, and k_e and k_L refer to the electronic and lattice contributions to the total thermal conductivity k_T [1,6]. Achieving an ideal figure of merit (ZT) requires a substantial thermoelectric power factor (σS^2) and low total thermal conductivity (k_T). Presently, researchers are actively involved in endeavors aimed at enhancing the thermoelectric power factor and reducing the total thermal conductivity. These efforts are based on a comprehensive understanding of the principles underlying thermoelectricity [7–9]. The deployment of energy filtration and the incorporation of dislocations and point defects are effective strategies for reducing total thermal conductivity. Previous studies have demonstrated the efficacy of these tactics in augmenting multi-wavelength phonon scattering, and they have also been suggested as a means to raise power factor. Novel thermoelectric materials exhibiting favorable ZT values are now under development, leading to the emergence of revolutionary technological breakthroughs [9]. The determination of a material's suitability as a thermoelectric (TE) material is contingent upon its bandgap and stability, as evidenced by the extant body of literature [10]. Nevertheless, there has been a growing interest in bismuth-based compounds in the past few decades because of their remarkable thermoelectric figure of merit (ZT). Due to their wide range of physical, chemical, and catalytic properties, these compounds

* Corresponding author. Department of Physics, Faculty of Science, University of M'sila, 28000 M'sila, Algeria.
** Corresponding author. Department of Physics, Faculty of Science, University of M'sila, 28000 M'sila, Algeria.
E-mail addresses: charifizoulikha@gmail.com, zoulikha.charifi@univ-msila.dz (Z. Charifi), baaziz_hakim@yahoo.fr, hakim.baaziz@univ-msila.dz (H. Baaziz).

https://doi.org/10.1016/j.mssp.2023.108048
Received 12 October 2023; Received in revised form 23 November 2023; Accepted 7 December 2023

have garnered significant interest among scientists and researchers

The categorization of TE materials is based on their operational temperature range, which can be divided into three distinct categories: ambient, mid-, and high-temperature. Bismuth telluride (Bi_2Te_3) and its alloys ($Bi_{2-x}Sb_{2x}Se_yTe_{3-y}$) have been identified as highly favorable bulk thermoelectric (TE) materials for applications in the ambient temperature range. This is primarily due to their exceptional thermoelectric figures of merit, ZT. The semiconductor $BiGaIn_2S_6$ satisfies the requirements of composite materials that incorporate abundant non-toxic components. Additionally, the material exhibits photovoltaic properties, including notable absorption coefficients, a moderate bandgap, and favorable durability. Furthermore, a notable deficiency in valuing these resources was seen. Hence, the efficacy of many methodologies employed in analogous ternary compounds, such as $AgBiS_2$, including alloying, doping, ligand surface modification, appropriate semiconductor alignment, and the formation of bulk heterojunctions, remains largely uninvestigated [11–14]. Future studies may find interest in exploring these research areas, which have the potential to further enhance gadget efficiency using a rich and non-toxic chemical. Bismuth-based materials, such as photo-detectors, offer various applications for other optoelectronic devices [15–17]. Furthermore, these materials can be employed in photocatalytic processes, such as the generation of solar-driven hydrogen and the degradation of light pollutants [18–20]. Furthermore, aside from the above mentioned uses, empirical evidence has shown that they exhibit practicality in the realm of batteries and thermoelectric devices that function using sustainable energy sources [21–24]. Moreover, therapeutic devices have employed them, particularly in the context of photothermal applications and bioimaging [25–27]. Each of these disciplines will possess an enhanced capacity to comprehend and improve the properties of materials containing bismuth.

The compound $BiGaIn_2S_6$, characterized by a narrow bandgap, exhibits low thermal conductivity, a potentially high Seebeck coefficient, and electrical conductivity. Hence, it is regarded as an advantageous thermoelectric material. The Bi_2S_3 material, when doped with $BiCl_3$, exhibits a noteworthy figure of merit ZT of 0.60, rendering it highly intriguing [24]. Heavy metal-based power semiconductors find application in diverse fields such as scintillation semiconductors, catalysts, thermoelectricity, and photovoltaics [28,29].

This study focuses on the computation and interpretation of key variables, including lattice parameters, compressibility modulus, and electronic structure. The aim is to provide a clearer understanding of chemical bonding and optical features. Given the potential application of this material in photovoltaic systems, it is imperative to calculate the optical properties. Furthermore, the Boltzmann transport theory offers predictions regarding thermoelectric transport parameters under the assumption of constant relaxation. These coefficients can be valuable for experimentalists in their endeavour to develop innovative and efficient thermoelectric materials. It is demonstrated that this material exhibits a low thermal conductivity, a significant Seebeck coefficient, and exceptional electrical conductivity. Consequently, the ZT value of these materials can reach 0.9, which is comparable to the ZT values of currently utilized thermoelectric materials. To the best of our knowledge, there is currently no existing theoretical or experimental research available on the TE compound $BiGaIn_2S_6$. Therefore, the findings presented in this study should be regarded as speculative predictions. The paper is structured into three distinct sections. Section 1 provides an overview of the introduction, Section 2 presents a comprehensive elucidation of the computational methodology utilized in the present investigation, and Section 3 examines the significant findings and conclusions that hold great significance in the realm of scientific inquiry at present.

2. Computational method

The results were obtained using Wien2k, a computational software based on density-functional theory (DFT) [30]. The structural properties were assessed utilizing the all-electron full potential linearized augmented plane wave (FP-LAPW) method, in conjunction with the Perdew and Wang local approximation (LDA) function [31]. The electronic and optical properties were evaluated by employing the modified Becke Johnson (mBJ) semi-local exchange potential [32], which is widely regarded as the most accurate approach currently available. Based on empirical evidence, it has been observed that the mBJ functional yields a more precise estimation of the band gap when compared to the commonly employed LDA/GGA functionals [33,34]. The potential under consideration exhibits independence from orbitals and possesses the capability to effectively forecast the band gap of diverse materials, including insulators, semiconductors, and transition metal oxides, with a strong degree of correlation [33,35]. The energy cut-off for the plane wave expansion was set at 400 Ryd, and the relaxation of the relative atomic positions was stopped when the energy level reached 10^{-4} Ryd. The calculations were performed in a self-consistent manner, following charge and atomic force convergence conditions of 0.001 e and 0.05 mRy/a.u, respectively. The determination of convergence in relation to the size of the basis is based on the calculation of the product between the minimum radius of the muffin-tin sphere and the maximum vector of the plane wave, which is denoted as $R_{MT}^{min} \times K_{MAX} = 9$. The computation of optical properties involved the utilization of a total of 20,000 k-points. The research used a plane wave cut-off of $G_{max} = 12$ (a.u) $^{-1}$ and examines R.M.T values ranging from 1.88 to 2.5 a.u for the elements *Bi*, *Ga*, *In*, and *S*. The computation of elastic constants is performed using the IRELAST technique [36], which is a component of the WIEN2k package. The determination of the Seebeck coefficient (*S*), electrical and thermal conductivities, and other thermoelectric properties of these materials is carried out via the semiclassical BoltzTraP technique [37]. The fundamental principles that form the basis of this code encompass the rigid band approximation and the concept of constant relaxation time. To optimize the effectiveness of investigating transport characteristics, a 100,000 k-point grid was employed. The relaxation time approximation can be used to calculate the transport coefficients (σ, *S*, and k_e) of the $BiGaIn_2S_6$ compound [38–40]:

$$\sigma = e^2 \sum_{\vec{k}} \left(-\frac{\partial f_0}{\partial E} \right) \tau_{\vec{k}} \vec{v}_{\vec{k}} \vec{v}_{\vec{k}} \quad (1)$$

where σ is the electrical conductivity, f_0 is the *Fermi* distribution function, $\tau_{\vec{k}}$ and $\vec{v}_{\vec{k}}$ represents the time of relaxation and the group velocity associated with $\vec{k}$ state. The coefficient of Seebeck is represented by,

$$S = eK_B\sigma^{-1} \sum_{\vec{k}} \left(-\frac{\partial f_0}{\partial E} \right) \tau_{\vec{k}} \vec{v}_{\vec{k}} \vec{v}_{\vec{k}} \left(\frac{\varepsilon_k - \mu}{K_B T} \right) \quad (2)$$

μ is the chemical potential and ε_k is the energy band. The electronic thermal conductivity contribution can be described as:

$$k_e = {K_B}^2 T \sum_{\vec{k}} \left(-\frac{\partial f_0}{\partial E} \right) \tau_{\vec{k}} \vec{v}_{\vec{k}} \vec{v}_{\vec{k}} \left(\frac{\varepsilon_k - \mu}{K_B T} \right)^2 - T\sigma S^2 \quad (3)$$

The evaluation of cubic elastic mechanical stability is conducted by employing the relaxed structure acquired by the LDA approximation. The thermodynamic parameters, specifically the Debye temperature (θ_D) and Grüneisen parameter (γ), were determined by evaluating the Gibbs functions using the Gibbs2 code [41] within the quasi-harmonic Debye models.

2.1. Structural and mechanical properties

Extensive research has been conducted on the ternary Bi (II) chalcogenides $Bi_2M_4X_8$ (where *M* represents *Al* or *Ga* and *X* represents *S* or *Se*) [42]. The innovative phase $BiGaIn_2S_6$ resulted from an attempt to partially substitute gallium with indium in the compound $Bi_2Ga_4S_8$; it is significantly distinct from the ternary bismuth indium sulfides that were

previously identified [43–46]. The quaternary sesquisulfide $BiGaIn_2S_6$ has a novel structure type (Pearson symbol: *mP20*). The results illustrated in Fig. 1 suggest that sulfur atoms fragment along the bidentate screw axes at 000 and 001/2. An undulating, layered structure parallel to (100) is formed by the densest sphere packing $(hc)_2$ and the stacking axis along [001]. Atoms of the elements *In* are situated in octahedral clouds, *Ga* atoms in tetrahedral clouds, and *Bi* atoms at the 2D layers' boundaries. Therefore, the layered structure is comprised of trigonal BiS_3 pyramids, InS_6 octahedra, and GaS_4 tetrahedra, which are all highly undulating. A portion of the *Ga* positions are occupied by *In* atoms in the homogeneity region. As an additional instructive instance of the structural impact of the sterically active lone electron pair of Bi^{III}, consider the formation of these corrugated layer bundles with the strong bonds *In–S*, *Ga–S*, and *Bi–S* within and their boundary formed by the outwardly oriented BiS_3 pyramids. During the curved van der Waals region between the layer bundles, these electron pairs are oriented parallel (100).

Table 1
Relaxed atomic positions predicted for $BiGaIn_2S_6$ with the LDA approximation.

Material	Atom	Atomic positions	
		Our study	*Experimental findings* [48]
$BiGaIn_2S_6$	***Bi***	**(0.5899, 0.25, 0.3875)**	**(0.5892, 0.25, 0.3848)**
	In (1)	**(0.7237, 0.25, 0.7577)**	**(0.7436, 0.25, 0.7758)**
	In (2)	**(0.9488, 0.25, 0.3568)**	**(0.9498, 0.25, 0.3585)**
	Ga	**(0.1668, 0.25, 0.9063)**	**(0.1718, 0.25, 0.9076)**
	S (1)	**(0.5381, 0.25, 0.7655)**	**(0.5150, 0.25, 0.7816)**
	S (2)	**(0.3446, 0.25, 0.4023)**	**(0.3588, 0.25, 0.3970)**
	S (3)	**(0.7785, 0.25, 0.1339)**	**(0.7336, 0.25, 0.1336)**
	S (4)	**(0.9684, 0.25, 0.7616)**	**(0.9583, 0.25, 0.7310)**
	S (5)	**(0.1429, 0.25, 0.0770)**	**(0.1418, 0.25, 0.0790)**
	S (6)	**(0.1412, 0.25, 0.6033)**	**(0.1559, 0.25, 0.5686)**

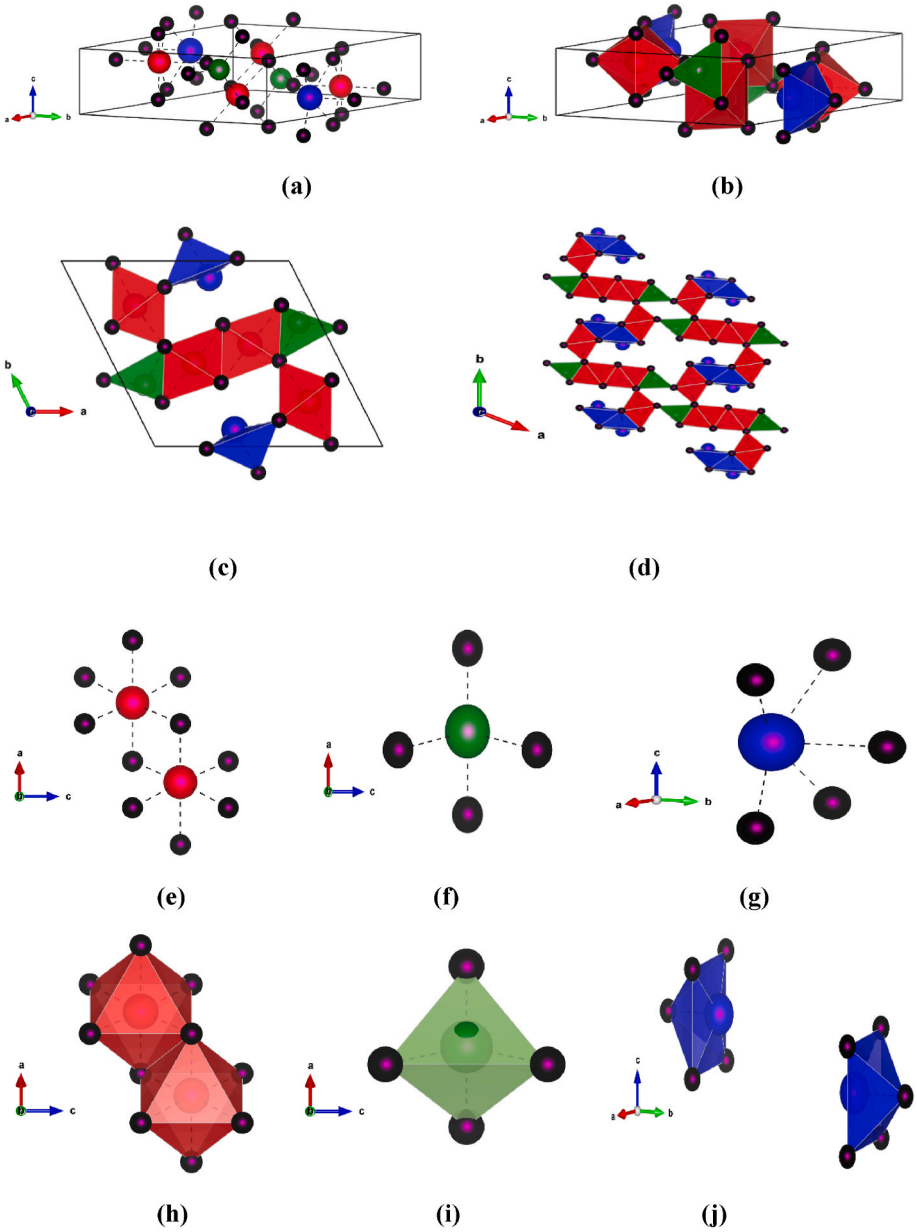

Fig. 1. Structure of the monoclinic $BiGaIn_2S_6$ ($P2_1/m$ space group) **(a)** The view is with respect to the (111) plane, **(b)**, **(c)** Groups of InS_6 octahedral geometry, GaS_4 octahedral geometry and BiS_7 groups view with respect to the (111), (110) plane, respectively, **(d)** supercell 2 × 2 × 2 of groups InS_6, GaS_4, and BiS_7. Black is *S*, Blue is *Bi*, Green is *Ga*, and Red is *In*.

Indeed, intermetallic phases may contain such configurations [47].

The objective of this inquiry is to optimize forces throughout various volumes, resulting in a comprehensive relaxation of the structure. Table 1 presents the results of the analysis conducted to compare the experimental outcomes with the predicted atomic locations of the materials using LDA approximations. The results of this computation align with the conclusions drawn from prior empirical investigations [48]. The comprehension of the structural attributes of solids holds great importance when examined at the microscopic level. Fig. 2 illustrates the energy projection for $BiGaIn_2S_6$ in relation to the conventional cell volume. The Murnaghan state formula [49] was utilized to derive structural properties by analyzing the volume-energy (E-V) data. In addition to the computed lattice constants a, b, and c, Table 2 provides a succinct summary of the experimental results [48]. It also includes the angle β, compressibility modulus B_0, and pressure derivative B'. The crystal structure of $BiGaIn_2S_6$ is distinguished by its monoclinic $P2_1/m$ space group. The lattice constants of $BiGaIn_2S_6$ have been calculated and found to $a = 12.2332$ Å (12.2809 Å [48]), $b = 11.1696$ Å (11.1207 Å [48]), $c = 3.7727$ Å (3.8062 Å [48]) and $\beta = 116.744°$ (116.305° [48]). The experimental data demonstrates a deviation of −0.389 % for the ratio $\Delta a/a$), 0.437 % for the ratio $\Delta b/b$), and −0.887 % for the ratio $\Delta c/c$). The current investigation details the physical parameters of the ground states, namely the E_{min}, B_0, and B' states, of bismuth-based quaternary compounds $BiGaIn_2S_6$. This document signifies the preliminary release of the research results. At this time, there is a lack of published data pertaining to the compressibility modulus of this material of interest. Potentially, the published results could serve as a foundation for subsequent efforts to experimentally characterize this novel compound. According to Table 2, the coordination of the *In* atoms and the *Ga* atoms is very irregular, probably a consequence of structural stresses. *In* (1) there is a (3 + 3) coordination with $\overline{d}(In1 - S) = 2.579$ Å and 2.648 Å (2.55 Å and 2.69 Å [48]), respectively. *In* (2) there is a (5 + 1) coordination with $\overline{d}(In2 - S) = 2.60$ Å and 2.71 Å (2.60 Å and 2.74 Å [48]), respectively. The mean distance from all individual values $\overline{d}(In - S) = 2.62$ Å (2.627 Å [48]), with seven times the standard deviation of the individual values, showing the significant distortions of the coordination octahedron. However, the mean value corresponds very well to the sum of the ionic radii for In^{3+} and S^{2-} (2.64 Å). Although it is larger than the sum of the covalence radii (2.54 Å), it is just as large as expected according to Pauling for the bond order PBO = 0.50. The octahedral tilt angles for a shared corner are 51°. The GaS_4 tetrahedra are also strongly distorted with $\overline{d}(Ga - S) = 2.331$ Å (2.345 Å [48]), *i.e.* with $\sigma(\overline{d}) = 5\sigma(d)$. This distance is 0.08 Å larger than in the Ga_2S_3 modifications [50] and is also greater than the sum of the ion radii or covalence radii (2.28 Å). Octahedral corners are shared at an angle of 63°–65°. The bismuth atoms are bonded with $\overline{d} = 2.644$ Å to three sulfur atoms. In addition, their subsequent coordination encompasses four sulfur atoms that are significantly further distant, with a bond length of $\overline{d} = 3.160$ Å (3.199 Å [48]). The complete BiS_7 coordination is shown in Fig. 1. The size and distortion of the tetrahedra are mainly determined by matrix effects, namely the arrangement of InS_6 octahedra and BiS_3 pyramids, as well as the position of the free electron pairs on the *Bi* atoms [48]. The structures of $Bi_2In_4S_9$ and $Bi_3In_5S_{12}$ also have networks of condensed InS_6 octahedra, InS_4 tetrahedra, and trigonal BiS_3 pyramids with extended (3 + 3) and (3 + 4) coordinations, respectively [43–46]. $Bi_2In_4S_9$ does not form a layered structure, but rather segments that form long [010] one-dimensional infinite chains separated from each other by regions with van der Waals interactions. $Bi_3In_5S_{12}$ forms a net-like structure of InS_6 octahedra and condensed *Bi–S* pyramids. The free spaces between the covalently bonded assemblies are determined by the lone pairs of electrons in *Bi* and *S*.

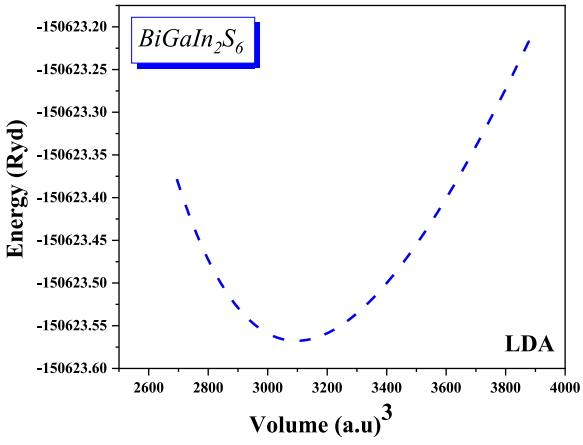

Fig. 2. $BiGaIn_2S_6$ total energy vs volume in the LDA approximation.

The evaluation of mechanical properties, such as second-order elastic constants (C_{ij}), and other relevant parameters, is essential in the manufacturing of solids for commercial purposes. Table 4 presents the anticipated numerical approximations for the 13 elastic rigidity components (C_{11}, C_{22}, C_{33}, C_{44}, C_{55}, C_{66}, C_{12}, C_{13}, C_{16}, C_{23}, C_{26}, C_{36}, and C_{45}), which were computed at 0 GPa using LDA, pertaining to the monoclinic symmetric compound $BiGaIn_2S_6$.The obtained results provide confirmation that the stability criteria described in equation (4) are met, thereby confirming the mechanical stability of the monoclinic structure of the material under investigation. Furthermore, as shown in Table 4, the magnitude of C_{33} is greater than that of C_{11} and C_{22}, suggesting that the material has a greater resistance to deformation along the *c*-axis than along the *a* or *b* axes. Based on the available research, an empirical investigation into the elastic coefficients of the compound in question has not yet been performed.

$$
\begin{aligned}
&C_{11} > 0,\ \ C_{22} > 0, C_{33} > 0,\ \ C_{44} > 0, C_{55} > 0,\ \ C_{66} > 0,\ \ [C_{11} + C_{22} + C_{33} + 2(C_{12} + C_{13} + C_{23})] > 0,\\
&\left[C_{33}C_{55} - (C_{35})^2\right] > 0,\ \ \left[C_{44}C_{66} - (C_{46})^2\right] > 0,\ \ [C_{22} + C_{33} - 2C_{23}] > 0,\\
&\left[C_{22}\left(C_{33}C_{55} - (C_{35})^2\right) + 2C_{23}C_{25}C_{35} - C_{55}(C_{23})^2 - C_{33}(C_{25})^2\right] > 0,\\
&\left\{\begin{array}{l} 2[C_{15}C_{25}(C_{33}C_{12} - C_{13}C_{23}) + C_{15}C_{35}(C_{22}C_{13} - C_{12}C_{23}) + C_{35}C_{25}(C_{11}C_{23} - C_{12}C_{13})] \\ -\left[\begin{array}{l} (C_{15})^2\left(C_{22}C_{33} - (C_{23})^2\right) + (C_{25})^2\left(C_{11}C_{33} - (C_{13})^2\right) + (C_{35})^2\left(C_{11}C_{22} - (C_{12})^2\right) \\ +C_{55}\left(C_{11}C_{22}C_{33} - C_{11}(C_{23})^2 - C_{22}(C_{13})^2 - C_{33}(C_{12})^2 + 2C_{11}C_{13}C_{23}\right) \end{array}\right] \end{array}\right\} > 0
\end{aligned}
\tag{4}
$$

The calculation of supplementary elastic constants for monoclinic structures, such as anisotropy (A_1, A_2, and A_3), bulk modulus (B), shear modulus (G), and Young modulus (E), was performed employing the formulae described in our previous publication [51]. The current

Table 2
Theoretical and experimental structural parameters using LDA of the quaternary compound $BiGaIn_2S_6$.

$BiGaIn_2S_6$	
Our results	***Experimental data*** [48]
$a = 12.2332$ Å	**12.2809 Å**
$b = 11.1696$ Å	**11.1207 Å**
$c = 3.7727$ Å	**3.8062 Å**
$\beta = 116.744°$ $b/a = 0.9130$	**116.305°**
$c/a = 0.3083$	**465.900 Å^3**
$B_0 = 80.0759$ GPa	
$B' = 5.0061$ $(\Delta a/a)_{EXP} = -0.389$ %	
$(\Delta b/b)_{EXP} = 0.437$ %	
$(\Delta c/c)_{EXP} = -0.887$ %	
$V_0 = 458.779$ Å^3	
$E_0 = -150623.5676$ Ryd	

Table 3
Selected interatomic distances (Å) and angles (deg) in the quaternary compound $BiGaIn_2S_6$.

Compounds	Distances and angles between atoms	Our LDA-based computations	Resulting Experiments [48]
$BiGaIn_2S_6$	***Ga–S (× 1)***	**2.271 Å**	**2.272 Å**
	Ga–S (× 2)	**2.329 Å**	**2.336 Å**
	Ga–S (× 1)	**2.393 Å**	**2.403 Å**
	Bi–S (× 1)	**2.628 Å**	**2.632 Å**
	Bi–S (× 2)	**2.653 Å**	**2.654 Å**
	Bi–S (× 2)	**3.080 Å**	**3.124 Å**
	Bi–S (× 2)	**3.241 Å**	**3.248 Å**
	In (1)-S (× 2)	**2.572 Å**	**2.582 Å**
	In (1)-S (× 1)	**2.595 Å**	**2.595 Å**
	In (1)-S (× 2)	**2.615 Å**	**2.622 Å**
	In (1)-S (× 1)	**2.714 Å**	**2.743 Å**
	In (2)-S (× 1)	**2.520 Å**	**2.532 Å**
	In (2)-S (× 2)	**2.569 Å**	**2.574 Å**
	In (2)-S (× 2)	**2.675 Å**	**2.677 Å**
	In (2)-S (× 1)	**2.714 Å**	**2.698 Å**
	S–In (1)-S (× 2)	**85.319°**	
	S–In (1)-S (× 2)	**86.200 °**	
	S–In (1)-S (× 2)	**86.616°**	
	S–In (1)-S (× 2)	**87.085°**	
	S–In (1) -S (× 1)	**89.646°**	
	S–In (1) -S (× 1)	**96.927 °**	
	S–In (1) -S (× 2)	**100.500°**	
	S–In (2)-S (× 1)	**83.3980°**	
	S–In (2)-S (× 1)	**89.2399°**	
	S–In (2)-S (× 1)	**92.2452°**	
	S–In (2)-S (× 1)	**92.2947°**	
	S–In (2) -S (× 1)	**93.2468°**	
	S–In (2) -S (× 1)	**95.1119°**	
	S-Ga-S (× 1)	**100.1425°**	
	S-Ga-S (× 1)	**110.2027°**	
	S-Ga-S (× 1)	**110.4826°**	
	S-Ga-S (× 1)	**116.6357°**	
	S–Bi–S (× 1)	**75.5175°**	
	S–Bi–S (× 1)	**76.8055°**	
	S–Bi–S (× 1)	**86.2871°**	
	S–Bi–S (× 1)	**91.7053°**	
	S–Bi–S (× 1)	**94.0574°**	

investigation utilized the Hill-model [52,53], a mathematical framework that calculates the average of the Voigt [54] and Reuss [55] mathematical models, in order to determine the additional elastic constants. In Table 5, the subscripts "V", "R", and "H" are utilized to denote the Voigt, Reuss, and Hill approximations, respectively.

The bulk modulus (B) of a material, under the influence of pressure, is a measure of the material's ability to withstand changes in volume. The shear modulus (G) is indicative of the crystal's capacity to resist plastic deformation, whereas a high B value is suggestive of favorable crystal strength. Table 5 presents evidence of the congruence between the bulk modulus estimated using the elastic constants within the Voigt-Reuss-Hill framework ($B_H = 79.206$ GPa) and the bulk modulus obtained

Table 4
Elastic constants of $BiGaIn_2S_6$ within the LDA approach.

Our results	$BiGa_2S_4$
C_{11}	**138.9682 GPa**
C_{22}	**125.8726 GPa**
C_{33}	**145.9403 GPa**
C_{44}	**39.4365 GPa**
C_{55}	**49.3869 GPa**
C_{66}	**40.7703 GPa**
C_{12}	**43.9398 GPa**
C_{13}	**57.7787 GPa**
C_{16}	**22.282 GPa**
C_{23}	**51.0406 GPa**
C_{26}	**12.614 GPa**
C_{36}	**11.524 GPa**
C_{45}	**15.085 GPa**
T_m	**1359.07 ± 300**
A_1	**0.9314**
A_2	**1.1638**
A_3	**0.9215**

Table 5
Modules of elasticity of $BiGaIn_2S_6$ utilizing the LDA estimation.

Our findings	$BiGaIn_2S_6$
B_V	**79.588**
B_R	**78.825**
B_H	**79.206**
G_V	**43.119**
G_R	**42.719**
G_H	**42.919**
E_V	**109.569**
E_R	**108.547**
E_H	**109.058**
σ_V	**0. 270**
σ_R	**0. 270**
σ_H	**0. 270**
B_H/G_H	**1.8454**
A_B	**0.4816**
A_G	**0.4659**
A^u	**0.05649**
V_t	**2913.76**
V_l	**5195.01**
V_m	**3242.74**
Θ_D	**339.393**

through total energy minimization approximations ($B_0 = 80.0759$ GPa) (see Table 2) for the material under consideration. Moreover, the G_H value for $BiGaIn_2S_6$ is 42,919.9 GPa. As a consequence, our compound has a substantial compressive capacity in comparison to its tensile strength. Pugh's ratio (B/G) [56] is utilized to ascertain the ductility or brittleness of a given material. According to Ref. [57], the crystal's ductility is contingent upon a B_H/G_H ratio exceeding 1.75, otherwise it exhibits brittleness. Table 5 displays the estimated B_H/G_H of the $BiGaIn_2S_6$ compound, suggesting that the compound is ductile. Frantsevich et al. employed Poisson's ratio (σ) to distinguish between brittleness and ductility, with a critical value of 0.26 applicable to both properties. The compound's brittleness is observed when the value of σ falls below 0.26, while its ductility is noted when the value of σ exceeds 0.26. The compound $BiGaIn_2S_6$ exhibits a calculated σ value of 0.27, suggesting its inherent ductility. The range of σ values for central forces in solids and ionic crystals is typically observed to be between 0.25 and 0.5. In contrast, covalent materials exhibit σ values ranging from 0.1 to 0.25, with interatomic forces falling under the category of non-central forces [58,59]. Based on the data shown in Table 3, it is evident that our material can be classified as exhibiting central forces. The statement mentioned above is corroborated by the Cauchy pressure [60], which is determined to be 4.50 ($C_p = C_{12} - C_{44}$). According to the Cauchy pressure values, the compound under investigation is ductile. The

identification of the ionic (covalent) character of the crystal bond can be accomplished by employing the positive (negative) Cauchy pressure value. The presence of positive Cauchy pressures in the quaternary compound $BiGaIn_2S_6$ provides evidence for its ionic character. The study carried out by Ref. [61] centered its attention on two thermodynamic variables, specifically the melting point T_m and Debye temperature (Θ_D), which are linked to the elastic properties of a material. Additionally, the study examined the longitudinal and transverse elastic velocities, denoted as v_l and v_t, respectively, and v_m is their average velocity. It can be deduced from the data in the table that the velocity of propagation of elastic compression waves is greater than that of elastic shear waves.

There are numerous physical mechanisms in which the elastic anisotropy of crystals can have a significant impact, including anisotropic deformation caused by plasticity, fracture conduct, and elastic instabilities. In order to increase the mechanical strength of structural quaternary compounds for use in mobile applications, the calculation of elastic anisotropy is critical.

In order to quantify the degree of anisotropy in the atomic bonding across various planes, shear anisotropic factors are utilized. The determination of the shear anisotropy factor for the {100} shear planes situated between the <011> and <010> directions has been determined to be [62]:

$$A_1 = 4C_{44} / (C_{11} + C_{33} - 2C_{13}) \tag{5}$$

The value of the shear anisotropy factor pertaining to the {010} shear planes situated between the <101> and <001> directions is [62]:

$$A_2 = 4C_{55} / (C_{22} - 2C_{23} + C_{33}) \tag{6}$$

The shear anisotropy factor pertaining to the {001} shear planes existing between the <110> and <010> directions has been reported as [62]:

$$A_3 = 4C_{66} / (C_{11} - 2C_{12} + C_{22}) \tag{7}$$

The quantification of elastic anisotropy is achieved through the evaluation of the deviation of the anisotropy factors from a value of unity. According to the data presented in Table 4, the calculated values for A_1, A_2, and A_3 were determined to be approximately 0.9314, 1.1638, and 0.9216, respectively. The compound under investigation exhibits shear anisotropy. Specifically, the {100} shear planes located between the <011> and <010> directions demonstrate a greater degree of anisotropy in the shear anisotropic factor than the {001} shear planes located between the <110> and <010> directions, as well as the <010> directions and {010} shear planes located between the <101> and <001> directions. Unfortunately, the lack of empirical evidence prevents any valid comparison of the conclusions reported in this study.

Chung and Buessem [63] have presented a theoretical framework that establishes the idea of percentage elastic anisotropy as a metric to quantify the extent of elastic anisotropy demonstrated by a crystal. The anisotropy percentages for compressibility and shear are presented as follows:

$$\begin{cases} A_B = (B_V - B_R)/(B_V + B_R) \times 100 \\ A_G = (G_V - G_R)/(G_V + G_R) \times 100 \end{cases} \tag{8}$$

In the context of these two equations, a numerical value of zero denotes the state of elastic isotropy, whereas a numerical value of one, signifying 100%, corresponds to the utmost conceivable degree of anisotropy. The values of A_B and A_G, as shown in Table 5, are 0.481 and 0.465, respectively. The compound under investigation has a notable characteristic of having a relatively low level of anisotropy in both the shear modulus and the bulk modulus.

Ranganathan and Ostoja-Starzewshi [64] present an alternate methodology for characterizing anisotropy. This technique entails acknowledging the tensorial properties of elastic stiffness and considering all stiffness coefficients, rather than solely relying on the ratios of individual coefficients. The mathematical representation of the universal anisotropy index, a parameter utilized to measure the extent of elastic anisotropy in a single crystal, can be expressed as follows:

$$A^U = 5\frac{G_V}{G_R} + \frac{B_V}{B_R} - 6 \tag{9}$$

The value of A^U is zero for single crystals that exhibit local isotropy. The degree of anisotropy in a single crystal is denoted by the deviation of A^U from zero. Universal anisotropy indicates that $BiGaIn_2S_6$ possesses a minimal degree of anisotropy, as A^U is 0.056.

The above-mentioned research is inadequate to comprehensively characterize the elastic properties of a crystal. Surface constructions that exhibit the reciprocal of Young's modulus in directions and linear compressibility are practical.

Linear compressibility of the monoclinic system is [65]:

$$\beta = n_1^2(S_{11} + S_{12} + S_{13}) + n_2^2(S_{12} + S_{22} + S_{23}) + n_3^2(S_{13} + S_{23} + S_{33}) + n_3 n_1(S_{15} + S_{25} + S_{35}) \tag{10}$$

S_{ij} are the elastic constants of deformability, and n_1, n_2, n_3: are the directional cosines (in spherical coordinates) following *x, y* and *z* respectively.

In the monoclinic system, the reciprocal of Young's modulus E in the direction of the unit vector n_i is expressed as [65]:

$$E = \frac{1}{\Omega} \tag{11}$$

$$\Omega = \begin{pmatrix} n_1^4 S_{11} + 2n_1^2 n_2^2 S_{12} + 2n_1^2 n_3^2 S_{13} + 2n_1^3 n_3 S_{15} \\ + n_2^4 S_{22} + 2n_2^2 n_3^2 S_{23} + 2n_1 n_2^2 n_3 S_{25} + n_3^4 S_{33} + 2n_1 n_3^3 S_{35} \\ + n_2^2 n_3^2 S_{44} + 2n_1 n_2^2 n_3 S_{46} + n_1^2 n_3^2 S_{55} + n_1^2 n_2^2 S_{66} \end{pmatrix} \tag{12}$$

Fig. 3 (a)-(b) displays the projected linear compressibility values derived from the theoretical elastic constants for the compound $BiGaIn_2S_6$. Equation (10) provides a definition for a three-dimensional surface, where the distance from the origin of coordinates to the surface corresponds to the linear compressibility in a specified direction. The cubic system exhibits isotropic linear compressibility, leading to a spherical shape. The isotropic nature of linear compressibility is evidenced by the spherical form depicted in Fig. 3 (a)–(b). The elastic anisotropy is more pronounced in the (XY) plane compared to the (XZ) plane, and it is somewhat more than in the (X = Z) plane. In contrast, the linear compressibility in the (XZ) plane exhibits isotropic behavior.

The orientation dependent Young's modulus for the compound $BiGaIn_2S_6$ is depicted in Fig. 3 (c)–(d) using the elastic compliance constants. Equation (11) and equation (12) establish the definition of a closed surface in three dimensions, whereby the distance from the origin of coordinates to the surface is equivalent to the Young's modulus in a specified direction. In a system that exhibits perfect isotropy, the surface in question would assume a spherical shape. However, it is important to note that this is not the case even within the cubic system. The Young's modulus surface of our compound has a non-spherical shape. Consequently, the compound demonstrates a significant level of anisotropy as a consequence of the distinct bonding characteristics observed across adjacent atomic planes. The elastic anisotropy is more pronounced in the (XY) plane compared to the (X = Y) plane and the (XZ) plane. However, the compound exhibits nearly isotropic behavior in the (YZ) plane.

2.2. Electronic properties

The investigation of the electronic properties of the monoclinic $BiGaIn_2S_6$ compound was conducted through an analysis of its band structure and density of states (DOS). Fig. 4 displays the computed electronic band structure of the $BiGaIn_2S_6$ quaternary based-bismuth compound, which was analyzed along the high symmetry directions (Z-C-D-Γ-Y-A-Γ-E) within the *Brillouin Zone*. The band structure

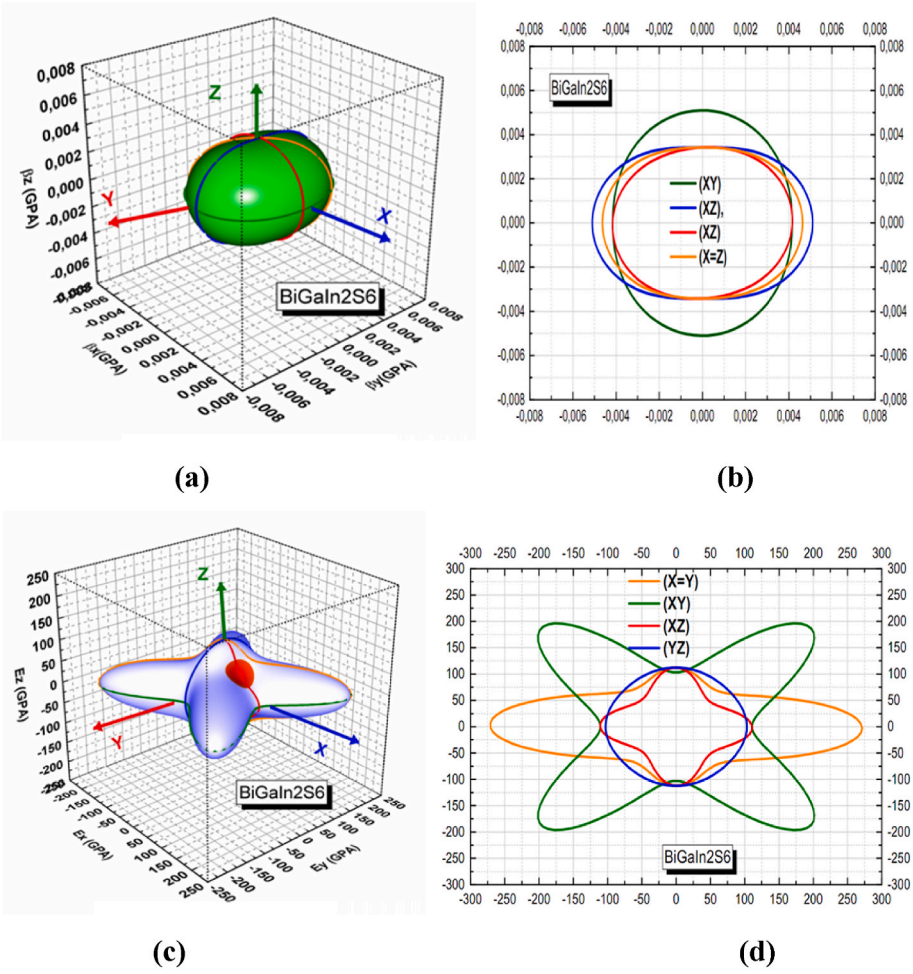

Fig. 3. Graphs of 3D surface of **(a)** the compressibility modulus, **(c)** the Young's modulus for $BiGaIn_2S_6$, and **(b),** and **(d)** their transverse sections in separated planes, respectively.

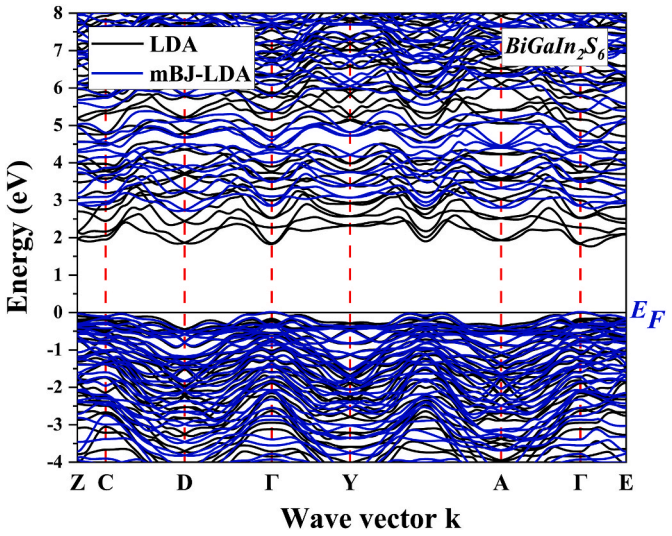

Fig. 4. The structure bands of $BiGaIn_2S_6$ using approximations of LDA, and mBJ-LDA.

predicted by the LDA approximation reveals a *Fermi* level situated at 0 eV, which signifies the semiconductor characteristics of the compound. The band gap prediction of 1.780 eV provides further evidence in favor of this characterization. Table 6 illustrates a significant improvement when the modified Becke-Johnson (mBJ) exchange potential is employed to address the underestimated band gap, as compared to LDA. Furthermore, it is important to highlight that the material being studied demonstrates an indirect band gap characteristic due to the existence of a distinct high symmetry K-point in the highest valence band Γ and the lowest conduction band Γ-E, as depicted in Fig. 4. Bismuth-based perovskites have improved material characteristics upon their incorporation. Extensive research efforts have been dedicated to the manipulation of bandgaps in bismuth perovskites, specifically. Considerable research effort has been devoted to the tuning of the bandgaps of bismuth perovskites. This is due to the fact that unaltered bismuth perovskites typically exhibit bandgaps exceeding 2 eV, which is suboptimal for achieving optimal performance in solar cells. An instance of this was illustrated in a study where the bandgap of $Cs_2AgBiBr_6$ was altered via pressure-induced modifications in its crystal structure [66]. Sulfur doping can reduce the bandgap of $Cs_3Bi_2I_9$ to a significantly more desirable value of 1.45 eV, as demonstrated by others [67,68]. A number of related bismuth halides have also been investigated in light of their potential as photovoltaic materials. As an illustration, dense $AgBi_2I_7$ films devoid of pinholes were produced by Kim et al. via spin coating silver and bismuth precursors followed by annealing. The material that was produced while remaining air-stable demonstrated a bandgap of 1.87 eV and solar cell efficiencies of up to 1.22 % [69]. Bismuth triiodide (BiI_3) has also demonstrated air stability, a bandgap of approximately 1.8 eV, and efficiency levels of up to 1.0 % [70–72]. Fig. 5 displays the total density of states (TDOS) and partial density of states (PDOS) of the quaternary compound $BiGaIn_2S_6$. The top of the valence band, ranging

Table 6
Values of energy gap *Eg* (eV), $\varepsilon_1(0)$ and $n(0)$ calculated for semiconductor $BiGaIn_2S_6$ with the LDA and mBJ-LDA approaches.

Quaternary compound	*Eg* (eV)			$\varepsilon_1(0)$			$n(0)$		
	LDA	mBJ-LDA	Exp (opt)		LDA	mBJ-LDA		LDA	mBJ-LDA
$BiGaIn_2S_6$	**1.780**	**2.711**	**1.9** [48]	ε_{1xx}	**9.193**	**6.461**	n_{xx}	**3.032**	**2.541**
				ε_{1yy}	**9.161**	**6.365**	n_{yy}	**3.026**	**2.523**
				ε_{1zz}	**9.720**	**6.785**	n_{zz}	**3.117**	**2.604**

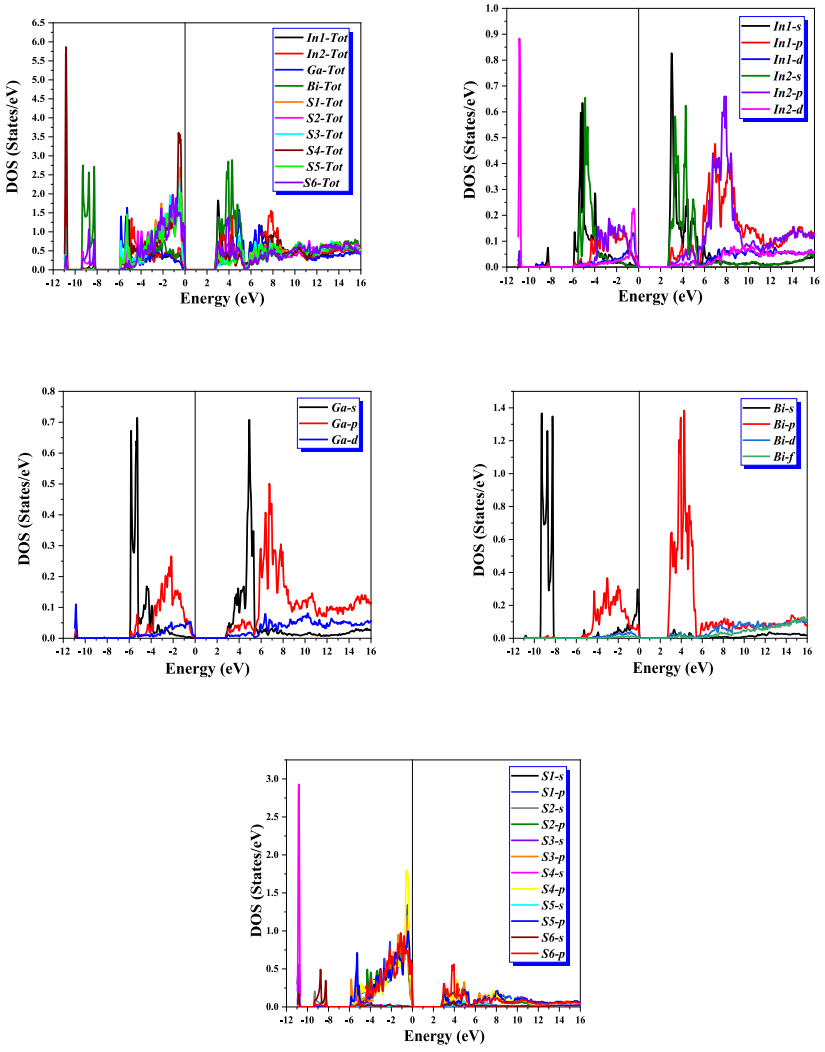

Fig. 5. The total and partial density of states of $BiGaIn_2S_6$ within mBJ-LDA.

from −6 to 0 eV, is formed by the contribution of the *Ga/S* atoms, with a minor contribution from *In* atoms. The lower of the valence band, ranging from −12 to −8 eV, is primarily influenced by *S* orbitals. The density of states graphs reveals that the bands within the energy range of 0–16 eV are attributed to the presence of *Bi/In* atoms. The hybridization of the bismuth atom with a minor contribution of indium atoms gives rise to the formation of bands that reside within the uppermost energy spectrum of the conduction band. High ELF values on the *Ga–S* and *In–S* bonds as well as on the three strong *Bi–S* bonds prove the covalent character of these bonds. The areas with the highest ELF values, however, belong to the lone electron pairs of the *S* atoms and *Bi* atoms. They project into the gaps of the layer structure and are crucial for the interlocked packing of the corrugated layers. Only van der Waals interactions exist between the layers. along with the weak Coulomb interactions of the further BiS_7 coordination [48].

2.3. Optical properties

The analysis of the optical properties of materials is an essential process in obtaining accurate information for utilization in optoelectronic and photovoltaic applications. The dielectric function is a crucial optical property that characterises the polarization and absorption mechanisms within a material. It also describes the manner in which a solid material reacts when subjected to electromagnetic radiation incident upon its surface. This statement elucidates the correlation between the electric field and the resultant polarization of the material. The dielectric function, $\varepsilon(\omega) = \varepsilon_1(\omega) + i\varepsilon_2(\omega)$, is a composite of two distinct components, namely the real $\varepsilon_1(\omega)$ and imaginary $\varepsilon_2(\omega)$ parts. The

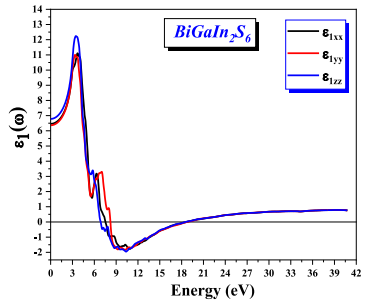

(a)

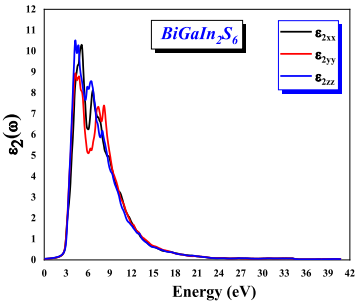

(b)

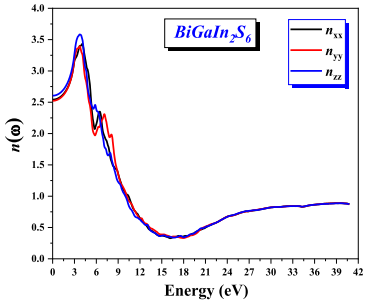

(c)

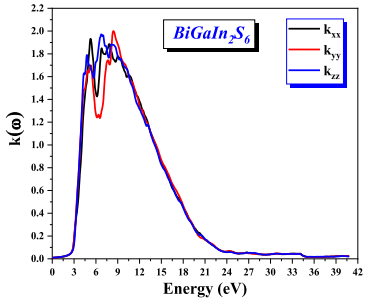

(d)

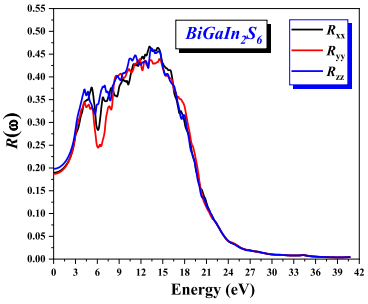

(e)

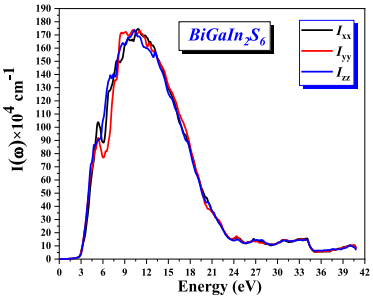

(f)

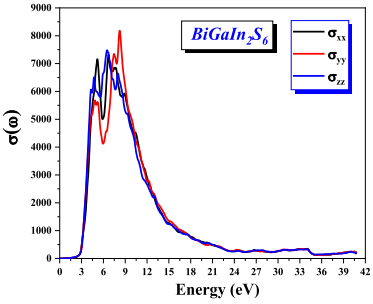

(g)

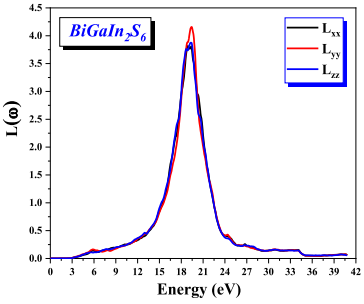

(h)

Fig. 6. **(a)** and **(b)** Alterations to the real and the imaginary functions of dielectrics, respectively, **(c)** the refractive index, **(d)** the extinction coefficient, **(e)** the reflectivity spectra, **(f)** the absorption coefficient, **(g)** the variations of optical conductivity, and **(h)** the energy loss function as a function of energy for $BiGaIn_2S_6$ within the mBJ-LDA approximation.

comprehension of the real and imaginary parts of the dielectric function enables the computation of significant optical parameters, including the refractive index $n(\omega)$ and the optical absorption coefficient $I(\omega)$, among others. The mBJ-LDA method is anticipated to yield a range of optical properties within the energy range of 0–42 eV. Our investigation in the monoclinic structure was exclusively centered on three discrete categories of polarization: extraordinary polarization (pertaining to fields oriented along the *x* or *y* axis), ordinary polarization (pertaining to fields directed along the *z* axis), and other forms of polarization were not displayed due to their relatively minor contributions.

The variation of the real component $\varepsilon_1(\omega)$ and imaginary component $\varepsilon_2(\omega)$ of the dielectric function of $BiGaIn_2S_6$ with respect to photon energy (ranging from 0 eV to 42 eV) is depicted in Fig. 6 (a)-(b). The real part, denoted as $\varepsilon_1(\omega)$, signifies the component of the dielectric constant that pertains to the storage of energy. The measurement quantifies the extent to which the material can undergo polarization when subjected to an externally applied electric field. A higher value of $\varepsilon_1(\omega)$ indicates a stronger polarization effect and an augmented potential for energy storage. On the other hand, the dissipation of energy, often known as losses, can be mathematically expressed as the imaginary component $\varepsilon_2(\omega)$. When $\varepsilon_2(\omega)$ has a value other than zero, it signifies that the material exhibits absorption characteristics by turning a fraction of the electric field's energy into thermal energy. The imaginary component is also associated with the conductivity of the material, which represents the facility with which electric charges can traverse it. The static dielectric constant, $\varepsilon_1(0)$, is referred to as such when the energy level is at zero. Table 6 presents the calculated values for $\varepsilon_1(0)$. Additionally, the anticipated band structures provide information regarding the inverse correlation between the aforementioned values and their respective band gaps. As a result, validation of Penn's model can be demonstrated [73]. In Fig. 6 (a), it can be shown that the principal peaks of $\varepsilon_1(\omega)$ for the investigated $BiGaIn_2S_6$ compound are situated within the visible spectrum. This is evident from the primary peaks observed along the *x*, *y*, and *z* axes with energy values of 3.7143 eV, 3.3606 eV, and 3.4694 eV, respectively, as calculated using mBJ-LDA calculations. Non-existence of diffusion is indicated by spectra which traverse zero. At these energy values, where the dispersion is zero and absorption is consequently highest, we have observed that the function $\varepsilon_1(\omega)$ for our compound becomes zero. The values of $\varepsilon_1(\omega)$ reach zero at energy levels of 7.5239 eV, 8.2042 eV, and 6.8708 eV, corresponding to the x, y, and z axes, respectively. Subsequently, the spectrum exhibits a negative trend, characterized by a minimum point, followed by a gradual decline until it reaches zero once again at 18.7622 eV.

Fig. 6 (b) depicts the changes of $\varepsilon_2(\omega)$ in relation to the energy of photons. According to Ref. [74], the dielectric function's imaginary component represents both the optical band gap and absorption characteristics. The analysis of these curves, which reflect the material's absorption, enables us to obtain diverse band transitions. The primary significant factors of the dielectric function are the fundamental absorption criteria, which begin at a value of 2.7075 eV. No significant absorption is detected within the energy range of up to 2.7 eV, suggesting that the optical band gap closely aligns with the electronic spectrum gap. Hence, there exists a correlation between the numerical values of the critical points and the transition from Γ to Γ-*E*. The sharp peaks observed in the $\varepsilon_2(\omega)$ curves serve as indicators of the electronic transitions that occur within our compound from the VBM to the CBM. Consequently, it is evident that the predominant peaks, which align with the highest level of absorption along the z-axis, are located at 4.2857 eV in close proximity to the fundamental peak. According to the findings, there is a notable peak observed within the UV spectrum. After reaching its maximum point, there is a notable decrease in values as the energy of photons increases.

The refractive index, a dimensionless quantity, is defined as the ratio of the velocity of light in vacuum to the velocity of light in any given medium. Additionally, it governs the extent of light refraction when entering a substance. The phase velocity is determined by the real part of the refractive index, while the extinction coefficient is influenced by the imaginary part of the refractive index. The extinction coefficient quantifies the degree of absorption loss experienced by a propagating wave in an optical medium. The computation of the refractive index $n(\omega)$ within the energy range of 0–42 eV is achieved by the equation $n(\omega) = \sqrt{\varepsilon_1(\omega)}$. As a result, the variable $n(\omega)$ exhibits similar features to those of $\varepsilon_1(\omega)$, as illustrated in Fig. 6 (c). The computed values for n (0) are presented in Table 6.

The refractive indexes of the compound at zero frequency are n_{xx} (0) = 2.541, n_{yy} (0) = 2.523, and n_{zz} (0) = 2.604, as ascertained by utilizing the mBJ-LDA approximation. As the frequency increases, the refractive index exhibits an increasing trend, reaching its highest at 4 eV, before decreasing to 18 eV. Further, it demonstrated attributes of non-linearity. To the best of our current understanding, there is a lack of empirical data available for the purpose of making comparisons. The results obtained suggest that the real part $\varepsilon_1(\omega)$ of the dielectric function and the refractive index exhibit a minor degree of anisotropy.

Fig. 6 (d) provides an illustration of the variation in the extinction coefficient $k(\omega)$ with respect to energy for the material being investigated. The spectra exhibit a maximum extinction coefficient value, which is associated with measured energies of 5.2109 eV, 8.3675 eV, and 6.7076 eV along the *x*, *y*, and *z* axes, respectively. Following the peak, there is a rapid decrease in the extinction coefficient as photon energies increase.

The term "reflectivity" refers to the ability of a material to reflect incident light that is directed onto its surface. The determination of reflectivity is defined by the ratio between the energy of photons reflected from a surface and the energy of photons incident upon the surface. Using mBJ-LDA, Fig. 6 (e) illustrates the energy-dependent reflectivity variation of our compound. The figure indicates that our semiconductor exhibits low reflectivity at low energies. The initial values are located at 18.9521 %, 18.6906 %, and 19.821 % along the *x*, *y*, and *z* axes, respectively. A rapid increase in reflectivity is observed at intermediate and high photon energies, with the maximal value being attained at approximately 13.1839 eV along the *z*-axis. These reflectivity maxima result from interband transitions. A reduction in reflectivity is correlated with an increase in energy.

The absorption spectra of the optical function play a crucial role in determining the depth of penetration of light with a given frequency into a material before it is absorbed. Additionally, it offers insights into the optimal efficiency of solar energy conversion. The concept pertains to the quantification of the level of light absorption exhibited by various materials. The spectrum of absorbance, acquired through the measurement of absorbance at various wavelengths or energy levels, can yield insights into the electronic transitions and structural properties of the material.

The absorption spectra of the optical function play a crucial role in determining the depth of penetration of light with a given frequency into a material before it is absorbed. Additionally, it offers insights into the optimal efficiency of solar energy conversion. The concept pertains to the quantification of the level of light absorption exhibited by various materials. The spectrum of absorbance, acquired through the measurement of absorbance at various wavelengths or energy levels, can yield insights into the electronic transitions and structural properties of the material. The variation of the absorption coefficient $I(\omega)$ with respect to photon energy is depicted in Fig. 6 (f). A similar pattern has been observed in relation to $\varepsilon_2(\omega)$. The provided figure depicts a notable increase in the absorption coefficient as the energy decreases. It is important to highlight that the peak value of this increase is detected at elevated energies. A significant peak in the "x" direction is seen at 10.925 eV. The absorption spectra show peaks with energies ranging from 4.91 eV to 17.89 eV. The presence of absorption peaks in the near-ultraviolet spectrum indicates that the material under research has absorption properties in this wavelength range. A thorough investigation of optical properties reveals remarkable photoelectric characteristics,

implying substantial potential for use in the absorber component of solar cells. Bi_2S_3 is classified as an *n*-type semiconductor [75], exhibiting a notable absorption coefficient within the range of 10^5 cm^{-1}. Furthermore, its absorption beginning occurs in the infrared spectrum. The bandgaps that have been reported are situated within the appropriate range for photovoltaic applications, ranging from 1.3 eV in bulk materials to 1.7 eV due to the influence of quantum confinement phenomena and/or differences in stoichiometry [76,77]. Ternary copper-bismuth sulphides exhibit varying stoichiometries and distinct characteristics. The orthorhombic structure is observed in the three extensively researched compounds, namely $CuBiS_2$, Cu_3BiS_3, and $Cu_4Bi_4S_9$. These compounds demonstrate notable absorption coefficients ranging from 10^4 to 10^5 cm^{-1} and possess *p*-type characteristics. The absorption onsets of these materials exhibit variations, and the documented bandgap values range from 1.5 to 2.62 eV for $CuBiS_2$, 1.2–1.84 eV for Cu_3BiS_3, and 0.88–1.14 eV for Cu_4Bi4S_9 [78,79]. In our study, the absorption coefficient values for *xx*, *yy*, and *zz* are 17.46 × 10^5 cm^{-1}, 17.37 × 10^5 cm^{-1}, and 17.36 × 10^5 cm^{-1}, respectively. Due to its exceptional optical characteristics, it demonstrates a significant degree of absorption intensity. Hence, it can be efficiently employed as a prominent candidate material for scaled optoelectronic devices.

The optical conductivity of the material is an optoelectrical phenomenon that facilitates the transport of electrons within the energy range of photons. The correlation between the current density $j(\omega)$ and the oscillating electric field $E(\omega)$ is indicated by certain features of the optical conductivity ($\sigma(\omega)$), as referenced in Ref. [80]. $\sigma(\omega)$ represents the electrical conductivity for $\omega \rightarrow 0$. There exists a direct connection between the imaginary part of $\varepsilon(\omega)$ and the real part of $\sigma(\omega) = \frac{\omega}{4\pi}\varepsilon_2$. The optical conductivity spectrum depicted in Fig. 6 (g) exhibits multiple peaks that correspond to the transitions between bands. Sharp edges are observed in the UV region when the energy level ranges between 4 and 12 eV.

The loss function of a material describes the rate at which an electron dissipates its energy as it traverses through the material. As previously noted in the literature [81,82], it is possible to derive the energy loss function $L(\omega)$ using the dielectric function $\varepsilon(\omega)$. The energy loss spectra of $BiGaIn_2S_6$ display significant magnitudes within the energy interval of 17.67–20.72 eV. At an energy of 19.41 eV, a distinct peak is observed along the *y*-axis. Note that for $BiGaIn_2S_6$ semiconductor, the major peak occurs when $\varepsilon_2(\omega)$ is very small and $\varepsilon_1(\omega)$ reaches zero again. The plasma frequency ω_p is the mean peak of the energy loss function. The frequency plasma ω_p for $BiGaIn_2S_6$ is observed to be 2.9488 × 10^{16} s^{-1}.

2.4. Thermoelectric response

The escalating need for energy has prompted scientific researchers to explore new materials and gadgets that exhibit high efficiency in converting thermal power into electrical power. Thermoelectric materials (TE) possess the potential for utilization in this specific case. These materials are capable of harnessing the Seebeck or Peltier effect [83], making them valuable for power generating purposes. Therefore, TE materials exhibit a wide range of possible uses in energy gadgets [84, 85]. An ideal thermoelectric material possesses a low thermal conductivity, denoted as *k* in units of W/mK, a high electronic conductivity, represented as σ in units of $(\Omega\ m)^{-1}$, and a high Seebeck coefficient, denoted as *S* in units of μV/K [86]. On the contrary, the thermal conversion power is derived from the power factor (PF)=$S^2\sigma$ and the figure of merit (ZT). This study focuses on the determination of different thermoelectric parameters such as carrier concentration (*n*), (σ), (k_e), (*S*), and (ZT) for $BiGaIn_2S_6$. These properties are analyzed using the semiclassical Boltzmann transport model implemented in the BoltzTrap package [37]. Additionally, the lattice thermal conductivity (k_L) is evaluated using Slack's equation [87]. The parameters are graphed as a function of temperature in Fig. 7. Due to the sensitivity of these properties to *Brillouin zone* sampling, in order to achieve accurate convergence, we employed the approximation of a constant relaxation time

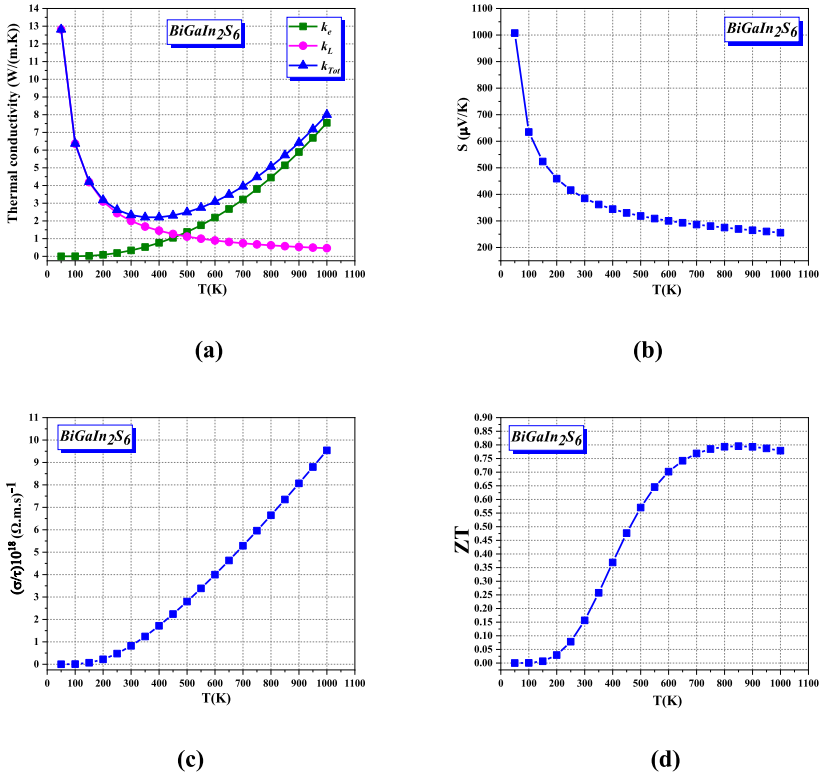

Fig. 7. Temperature dependence of **(a)** the total thermal conductivity k_{Tot}, the lattice thermal conductivity k_L and electronic thermal conductivity k_e, **(b)** the Seebeck coefficient *S*, **(c)** the electrical conductivity per relaxation time (σ/τ), **(d)** the figure of merit *ZT* of $BiGaIn_2S_6$ within the mBJ-LDA approximation.

(10^{-14} s) in conjunction with a dense mesh consisting of 100,000 k-points within the *Brillouin zone*.

Fig. 7 (a) display the thermal conductivity components k_L and k_e, which together constitute the total thermal conductivity k_T. The k_e for the $BiGaIn_2S_6$ compound has been determined and is presented in Fig. 7 (a). Based on the plot, it can be inferred that the value of k_e for the compound under investigation exhibits a direct relationship with temperature. The value experienced a significant increase, rising from 0.33 (W/mK) to 7.54 (W/mK) when temperature is elevated from 300 K to 1000 K, respectively. The electrical conductivity of $Bi_{2-x}Sb_xTe_3$ obtained were 80.018 S/m (at 440 K) for MW-Bi_2Te_3 and 27.504 S/m (at 523 K) for MW-$Bi_{0.5}Sb_{1.5}Te_3$, respectively, while MA-Bi_2Te_3 and MA-$Bi_{0.5}Sb_{1.5}Te_3$ Seebeck coefficients values of 75 S/m (at 460 K) and 16.7 S/m (at 300 K), respectively, as *n*- and *p*-type [91]. The k_L parameter is a fundamental thermal property of solids that serves to quantify the heat conduction mechanism through the oscillatory motion of lattice ions, also known as phonons, within solids. The computation of k_L for $BiGaIn_2S_6$ throughout the temperature range of 50–1000 K was performed using the renowned Slack's model [87,88], as depicted in Fig. 7 (a). The k_L values of $BiGaIn_2S_6$ at 300 K and 1000 K are 1.9969 W/mK and 0.4579 W/mK, respectively. The Debye temperature (θ_D) and Grüneisen parameter (γ) for the $BiGaIn_2S_6$ compound at a temperature of 300 K were determined to be 343.95 K and 2.3364, respectively, using the Quasi-harmonic Debye approximation method [89]. This model provides the values of θ_D and γ at 0 K temperature and 0 GPa pressure, which were derived from the elastic constants [90]. According to the data presented in Fig. 7 (a), it is evident that the (k_L) of our compound exhibits a reduction as the temperature increases.

According to the data presented in Fig. 7 (a), it can be observed that the value of k_T exhibits a decreasing trend as the temperature increases, until it reaches approximately 350 K. This observation suggests a reduced level of phonon-phonon interaction in lower temperature regimes. At elevated temperatures, the interaction between phonons becomes more pronounced, leading to a decrease in the k_L values. The relatively low value of the thermal conductivity value of approximately 2.2069 W/(m.K) at a temperature of 350 K verifies its accuracy. The total thermal conductivity of $Bi_{2-x}Sb_xTe_3$ obtained were 0.876 W/mK (at 440 K) for MW-Bi_2Te_3 and 0.466 W/mK (at 523 K) for MW-$Bi_{0.5}Sb_{1.5}Te_3$, respectively, while MA-Bi_2Te_3 and MA-$Bi_{0.5}Sb_{1.5}Te_3$ attained total thermal conductivity values of 1.032 W/mK (at 460 K) and 1.742 W/mK (at 300 K), respectively, as *n*- and *p*-type [91]. In our case the calculated total thermal conductivity of $BiGaIn_2S_6$ is 2.33 W/mK at 300 K. This is in line with the experimental results [91]. One additional crucial parameter that elucidates the thermoelectric conversion of a substance is its Seebeck coefficient (*S*). The temperature-dependent *S* of the compound under investigation was calculated and plotted against temperature, as depicted in Fig. 7 (b). The figure displays the computed values of *S*, which demonstrate positivity throughout the entire temperature range. This suggests the presence of *p*-type charge carriers. So, the holes are presumed to be the dominant charge carriers, performing a pivotal role in the conduction process.*S* Furthermore, in the case of our semiconductor, the value of *S* exhibits a reduction as the temperature increases from 384.8363 μV/K at 300 K to 255.5554 μV/K at 1000 K. The Seebeck coefficients of $Bi_{2-x}Sb_xTe_3$ obtained were −160 μV K^{-1} (at 440 K) for MW-Bi_2Te_3 and 157 μV K^{-1} (at 523 K) for MW-$Bi_{0.5}Sb_{1.5}Te_3$, respectively, while MA-Bi_2Te_3 and MA-$Bi_{0.5}Sb_{1.5}Te_3$ Seebeck coefficients values of −148 μV K^{-1} (at 460 K) and 302 μV K^{-1} (at 300 K), respectively, as *n*- and *p*-type [91]. σ is used to represent the phenomenon of electron conduction in compounds. The energy band hypothesis elucidates that conductors possess readily available free charges that facilitate conduction, whereas semiconductors necessitate the input of external energy to generate charges. The plots of (σ/τ) for our compound, computed within the temperature range of 50 K–1000 K, are depicted in Fig. 7 (c). The data presented in the figure illustrates a positive correlation between temperature and the ratio of electrical conductivity to relaxation time (σ/τ). Specifically, the value of (σ/τ) rises from 0.8214 × 10^{18} (Ω m s)$^{-1}$ at a temperature of 300 K to 9.5384 × 10^{18} (Ω m s)$^{-1}$ at a temperature of 1000 K. Therefore, our semiconductor exhibits a great capacity for converting heat energy into electrical energy. An optimal thermoelectric (TE) material should exhibit a high electrical conductivity (σ) and a low thermal conductivity (k_T). The compound being examined in this study exhibits conformity to the criteria of an outstanding thermoelectric material. The evaluation of a material's potential in thermoelectric applications is not just decided by its power factor (PF) value, but rather by its figure of merit (ZT) value. Fig. 7 (d) displays the ZT plots obtained from the computational analysis of our compound. The semiconductor has a noteworthy maximum ZT value of 0.7953 at a temperature of 850 K, indicating its potential for advantageous utilization in thermoelectric applications. The *ZT* of $BiCl_3$-doped Bi_2S_3 has been measured to be 0.6 [24]. The thermoelectric characteristics of $Bi_{2-x}Sb_xTe_3$ samples were investigated. The greatest *ZT* values obtained were 1.04 (at 440 K) for MW-Bi_2Te_3 and 0.76 (at 523 K) for MW-$Bi_{0.5}Sb_{1.5}Te_3$ samples, respectively, while MA-Bi_2Te_3 and MA-$Bi_{0.5}Sb_{1.5}Te_3$ samples attained maximum ZT values of 0.74 (at 460 K) and 0.27 (at 300 K), respectively, as *n*- and *p*-type [91]. The semiconductor $BiGaIn_2S_6$ exhibits favorable values for S, k_T, σ, and ZT, rendering it an appealing candidate for sustainable energy production.

The objective of the following part of this research is to predict the values of σ/τ, k_e/τ, *S*, and ZT for different charge transport concentrations ranging from - 3 × 10^{22} cm^3 to 7 × 10^{22} cm^3 at temperatures of 300 K, 600 K, and 900 K. In Fig. 8 (a), the plot illustrates the relationship between the ratio (σ/τ) and the concentration of charge carriers for the $BiGaIn_2S_6$ semiconductor at three different temperatures: 300 K, 600 K, and 900 K. An increase in the concentration of holes will lead to a corresponding increase. The graphical representations of the function (σ/τ) at different temperatures offer empirical support for the temperature-independent nature of the function (σ). The reason for this phenomenon lies in the fact that the behaviour of the material is not influenced by its temperature but rather by the DOS, or transport patterns, within the solid. The compound under investigation exhibits a greater degree of delocalization in the conduction band compared to the valence band near the *Fermi* level [92]. This is supported by the observation of a smaller (σ/τ) value in *n*-type compounds relative to *p*-type compounds.

The graphs (k_e/τ) of the semiconductor $BiGaIn_2S_6$ are displayed in Fig. 8 (b). of the are presented in Fig. 8 (b). The data indicates that the value of (k_e/τ) increases as the concentration of charge carriers rises due to the introduction of hole doping. Conversely, the value of (k_e/τ) will decrease in response to an increase in electron concentration. The dependence of the value of the (k_e) on temperature has been noted, but the value of the (σ) remains unaffected. This phenomenon can be attributed to the positive correlation between the (k_e) and the temperature. However, σ does not appear to.

The Seebeck coefficients (S) are mainly affected by the temperature at high concentrations, showing a trend to decrease with the increase in temperature. The $BiGaIn_2S_6$ compound has the characteristics of a narrow bandgap; therefore, its *S* peak will be afected by the bipolar efect. The bipolar thermal efect is determined by the ratio of mobility of the minority carriers. The maximum absolute values of S gradually decrease and approach the higher carrier concentration regions with the increases in temperature. The magnitudes of the *S* values for *p*-type semiconductors are larger compared to those for *n*-type semiconductors, as depicted in Fig. 8 (c). Fig. 8 (d) depicts the variations in ZT curves that occur as a function of temperature and carrier concentration. These graphs demonstrate that the material possesses the properties of a thermoelectric semiconductor at elevated temperatures. The ZT values of *p*-type semiconductors are considerably higher than those of *n*-type. At 900 K, the *p*-type (*n*-type) compound has the highest ZT values of 0.9874 (0.6478) with 14.2449 × 10^{20} cm^3 (−3.3849 × 10^{20} cm^3). The promising results derived from these ZT values indicate that the compound has a great deal of potential for use as a thermoelectric material. *n*-type-$Bi_2Al_4Se_8$ has a ZT of 0.76 when $n = -6.448 \times 10^{18}$ cm^3 [93], ZT∼

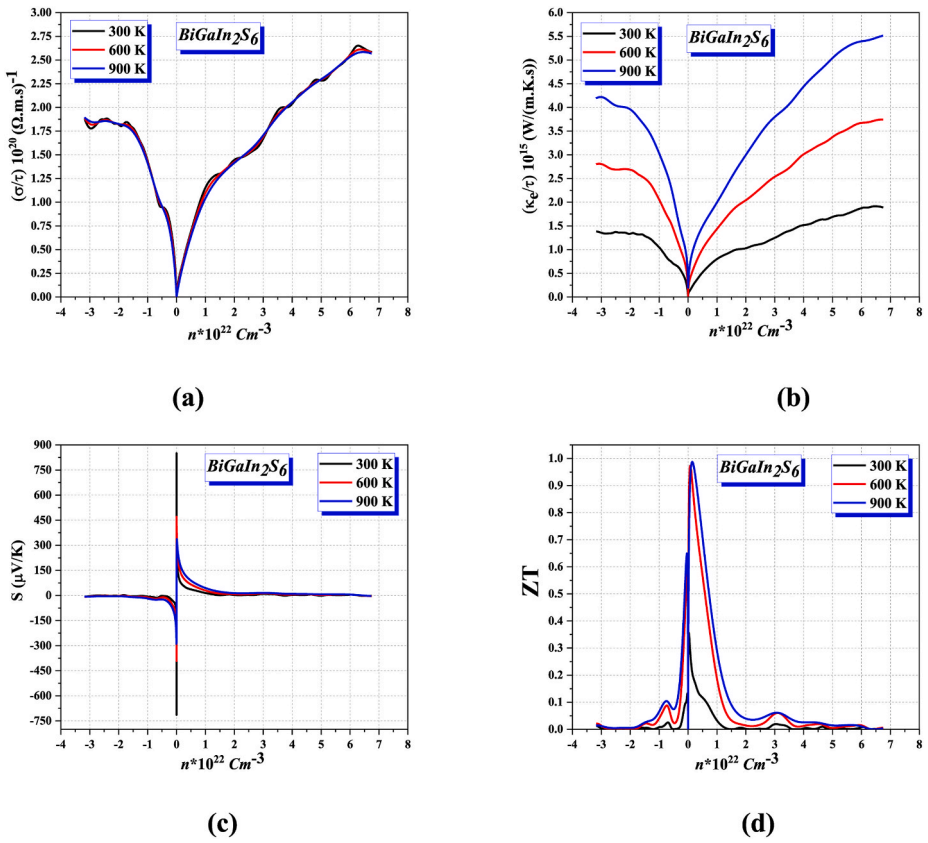

Fig. 8. The estimated **(a)** electrical conductivity per relaxation time (σ/τ), **(b)** electronic thermal conductivity per relaxation time (k_e/τ), **(c)** Seebeck coefficient S and **(d)** figure of merit ZT versus charge carrier concentration for T = 300, 600, and 900 K via the mBJ-LDA approach of $BiGaIn_2S_6$.

0.99 ($CuPN_2$: $n = -1.7 \times 10^{19}cm^3$) for n-type, (HPN_2: $n = 1.4 \times 10^{19}cm^3$) for p-type, $LiPN_2$ or $NaPN_2$ ($n = 0.4 \times 10^{19}cm^3$) for p-type [81, 94], and at 700 K, $CaZn_2Sb_2$ has a ZT of 0.33 [95]. For the n-type of $LiCrZ$ ($Z = S$, Se, and Te), ZT is 0.68, 0.9495, and 0.9507, respectively [96]. For $CoFeTiGe$ ($CoFeCrGe$), ZT = 0.25 and 0.404 (0.243 and 0.644) for n and (p)-types, respectively [97]. Maximum ZT readings in the spin-down directions are 0.81355 for $RbCrS$, 0.62249 for $RbCrSe$, and 1.02846 for $RbCrTe$ [98] and for the DHH $ScNbNi_2Sn_2$ ZT reaches 0.6391 when T = 900 K [99].

After successfully showcasing the notable thermoelectric capabilities of $BiGaIn_2S_6$, we proceed to calculate (S, (σ/τ), (k_e/τ)) along the x, y, and z axes utilizing the mBJ-LDA approach. The tensors $(\sigma_{xx} \neq \sigma_{yy} \neq \sigma_{zz})$, $(S_{xx} \neq S_{yy} \neq S_{zz})$, $(k_{e_{xx}} \neq k_{e_{yy}} \neq k_{e_{zz}})$ have a diagonal orientation.

In Fig. 9 (a), it can be shown that the S_{zz} Seebeck coefficient parameters for the compound $BiGaIn_2S_6$ exhibit somewhat lower values compared to the S_{xx} and S_{zz} parameters, except for the case when the temperature (T) is equal to 50 K, where the ordering is inverted. In contrast, the values of the S_{xx}, S_{yy} Seebeck coefficients exhibit a high degree of similarity. At a temperature of 300 K, the Seebeck coefficients are as follows: $S_{xx} = 413.3856$ μV/K, $S_{yy} = 420.2292$ μV/K, and $S_{zz} = 320.8942$ μV/K.

The percentage of $\sigma_{xx}(\sigma_{yy})$ at elevated temperatures of σ_{zz} for the semiconductor $BiGaIn_2S_6$ is 36.83 (64.70) percent, as evidenced by the notable density of states (DOS) associated with this particular orientation, as depicted in Fig. 9 (b). The electrical conductivity along the xx direction is found to be comparable to the electrical conductivity along the yy direction as the temperature varies within the range of 50 K–300 K. The differences between σ_{xx}, σ_{yy}, and σ_{zz} parameters become more apparent at higher temperatures.

Within the temperature range of 50 K–300 K (specifically 50 K–200 K), the electronic thermal conductivity in the xx (zz) direction is equal to the electronic thermal conductivity in the yy (xx, yy) direction. At elevated temperatures, the discrepancy among the aforementioned three values becomes more pronounced. Specifically, the value of $k_{e_{zz}}$ surpasses that of $k_{e_{xx}}$ and $k_{e_{yy}}$, with $k_{e_{xx}}$ ($k_{e_{yy}}$) being estimated to be 47.001 (78.4093) percent of $k_{e_{zz}}$ (see Fig. 9 (c)).

2.4.1. Methods for improving ZT

Fig. 10 (a) illustrates the variations in the thermoelectric figure of merit (ZT) of $BiGaIn_2S_6$ throughout a broad temperature spectrum ranging from 50 K to 1000 K. Our compound exhibits a thermoelectric figure of merit (ZT) of 0.7930 at a temperature of 900 K. This result corresponds to a carrier concentration (n_0) of 44.3235×10^{19} cm^{-3}. The semiconductor exhibits two distinct peaks in its figure of merit (ZT), with one peak corresponding to the n-type and the second peak corresponding to the p-type (see Fig. 10 (b)). The compound $BiGaIn_2S_6$ has a maximum ZT value of 0.9874 for the n-type and 0.6496 for the p-type at a temperature of 900 K, as depicted in Fig. 10 (b). This implies that there are noticeable differences in the thermoelectric characteristics between p-type and n-type materials. Therefore, the semiconductor under investigation exhibits the highest thermoelectric efficiency among the compounds of the n-type. The ZT value for $BiGaIn_2S_6$ is determined to be 0.5509 under the condition that the difference between the chemical potential (μ) and the reference chemical potential (μ_0) is equal to zero. This finding demonstrates that the thermoelectric properties of our compound exhibit high efficacy even in the absence of doping.

In order to maximise the ZT value, it is crucial to determine the optimal carrier concentration and temperature. It is advisable to investigate the impact of doping levels on the thermoelectric figure of merit (ZT) at a temperature of 900 K. Fig. 10 (c) demonstrates a maximum ZT value of 0.98741. In order to attain this value, the charge carrier concentration is increased to $n = 0.14494 \times 10^{22}$ cm^{-3} or when the chemical potential lowers to 0.47499 Ryd. The material under study

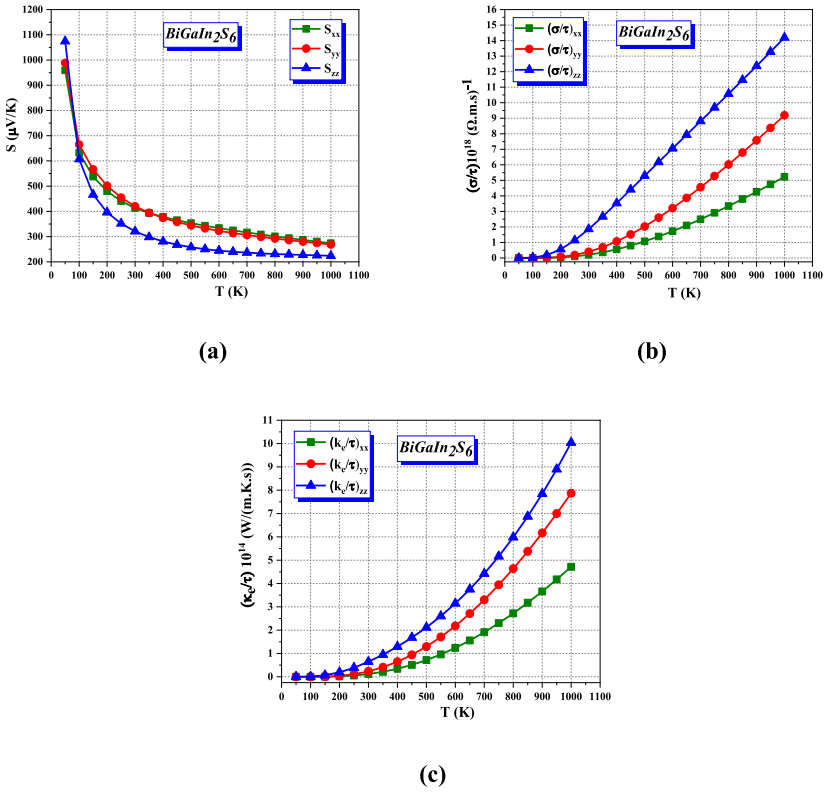

Fig. 9. Calculated anisotropic transport properties for $BiGaIn_2S_6$ **(a)** Seebeck coefficient tensor **(b)** ratio of electrical conductivity per relaxation time (σ/τ) tensor components, **(c)** ratio of the electronic thermal conductivity per relaxation time (k_e/τ) tensor components.

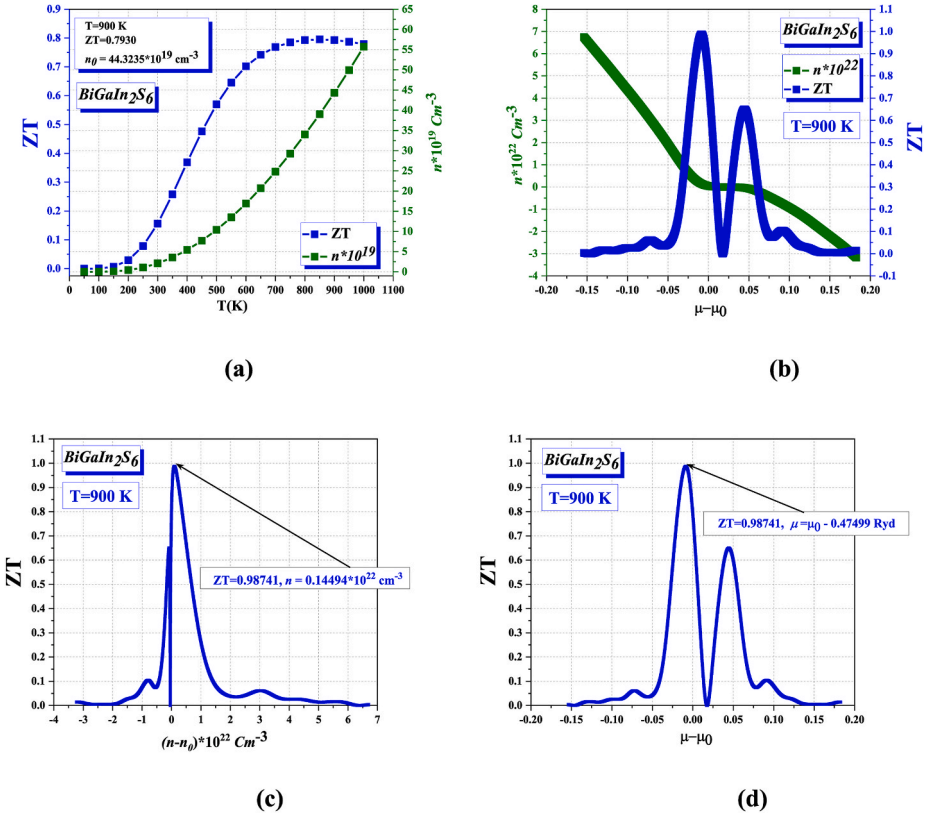

Fig. 10. The figure of merit *ZT* of $BiGaIn_2S_6$ as a function of (a), and (c) temperature and carrier concentration, (b), (d) chemical potential at fix temperature (T = 900 K).

shows potential applications in the thermoelectric field.

3. Conclusion

The present study offers a comprehensive examination of the structural, electronic, elastic, optical, and thermoelectric properties of $BiGaIn_2S_6$. The previously mentioned properties were computed utilizing the accurate density functional theory (DFT) theory, with the full-potential linearized augmented plane wave (FP-LAPW) method integrated into the Wein2k code. The computed lattice parameters demonstrate a significant resemblance to the presently accessible experimental findings. On the basis of the calculated electronic properties, it is possible to deduce that the investigated material possesses properties that are typical of a semiconducting material. By employing mBJ-LDA, it was determined that the compound demonstrated an indirect band gap (Γ→Γ-E) of 2.711 eV. On the basis of the elastic properties that were measured, it is possible to conclude that the investigated material exhibits anisotropy and ductility. The calculated optical coefficients offer further elucidation regarding the material $BiGaIn_2S_6$, which demonstrates a substantial absorption coefficient specifically in the ultraviolet region of the electromagnetic spectrum. Boltzmann theory and Slack's model were utilized to ascertain the thermoelectric characteristics of the $BiGaIn_2S_6$ compound at various temperatures. It was determined that our compound possesses a high electrical conductivity and a low lattice thermal conductivity. The positive Seebeck coefficient suggests that this material exhibits properties that align with the classification of a *p*-type material. The semiconductor $BiGaIn_2S_6$ has been identified as having a maximum ZT value of 0.98741. This phenomenon arises either when the concentration of charge carriers is increased to $n = 0.14494 \times 10^{22}\ cm^{-3}$ or when the chemical potential decreases to 0.47499 Ryd. The findings obtained from this research indicate that the material being studied exhibits potential for application in thermoelectric and optoelectronic devices.

CRediT authorship contribution statement

T. Ghellab: Writing – original draft, Methodology, Conceptualization. **Z. Charifi:** Writing – review & editing, Writing – original draft, Formal analysis, Data curation, Conceptualization. **H. Baaziz:** Supervision, Software, Methodology, Data curation.

Declaration of competing interest

The authors declare that they have no known competing financial interests or personal relationships that could have appeared to influence the work reported in this paper

Data availability

Data will be made available on request.

Acknowledgments

The authors (T. Ghellab, Z. Charifi and H. Baaziz) would like to thank the general directorate for scientific research and technological development for their financial support during the realization of this work.

References

[1] M.H. Elsheikh, D.A. Shnawah, M.F.M. Sabri, S.B.M. Said, M.H. Hassan, M.B. A. Bashir, M. A Mohamad, Renew. Sustain. Energy Rev. 30 (2014) 337–355.
[2] X.F. Zheng, C.X. Liu, Y.Y. Yan, Q. Wang, Renew. Sustain. Energy Rev. 32 (2014) 486–503.
[3] H. J. Goldsmid, H. J. Goldsmid, Morgan & Claypool Publishers: New York, NY, USA, (2017). .
[4] W.H. Steele, Science 562 (1893) 256.
[5] D. Champier, Energy Convers. Manag. 140 (2017) 167–181.
[6] N. Mingo, Appl. Phys. Lett. 84 (2004) 2652–2654.
[7] D.C. Nemir, J. Beck, J. Electron. Mater. 39 (2010) 1897–1901.
[8] L.-D. Zhao, S.-H. Lo, Y. Zhang, H. Sun, G. Tan, C. Uher, C. Wolverton, V.P. Dravid, M.G. Kanatzidis, Nature 508 (2014) 373–377.
[9] D.K. Aswal, R. Basu, A. Singh, Energy Convers. Manag. 114 (2016) 50–67.
[10] G.J. Snyder, E.S. Toberer, Mater. Sci. Eng. 7 (2010) 101–110.
[11] G.H. Carey, a.L. Abdelhady, Z. Ning, S.M. Thon, O.M. Bakr, E.H. Sargen, Chem. Rev. 115 (2015) 12732–12763.
[12] F. Liu, C. Ding, Y. Zhang, T.S. Ripolles, T. Kamisaka, T. Toyoda, S. Hayase, T. Minemoto, K. Yoshino, S. Dai, M. Yanagida, H. Noguchi, Q. Shen, J. Am. Chem. Soc. 139 (2017), 16708.
[13] M. Yuan, M. Liu, E.H. Sargent, Nat. Energy 1 (2016), 16016.
[14] C.R. Kagan, C.B. Murray, Nat. Nanotechnol. 10 (2015) 1013–1026.
[15] J. Chao, et al., Mater. Res. Bull. 98 (2018) 194–199.
[16] W. Huang, et al., Nanoscale 10 (2018) 2404–2412.
[17] H. Yu, et al., CrystEngComm 19 (2017) 727–733.
[18] A. Sarkar, et al., J. Colloid Interface Sci. 483 (2016) 49–59.
[19] X. Meng, Z. Zhang, J. Mol. Catal. Chem. 423 (2016) 533–549.
[20] H. Abdullah, D.-H. Kuo, J. Phys. Chem. C 119 (2015) 13632–13641.
[21] J. Ni, et al., Adv. Energy Mater. 4 (2014), 1400798.
[22] G. Nie, X. Lu, J. Lei, L. Yang, C. Wang, Electrochim. Acta 154 (2015) 24–30.
[23] W. Yang, H. Wang, T. Liu, L. Gao, Mater. Lett. 167 (2016) 102–105.
[24] K. Biswas, L.D. Zhao, M.G. Kanatzidis, Adv. Energy Mater. 2 (2012) 634–638.
[25] Y. Cheng, et al., Angew. Chem., Int. Ed. 57 (2018) 246–251.
[26] Y. Yang, et al., Part. Syst. Charact. 32 (2015) 668–679.
[27] Z. Li, et al., RSC Adv. 7 (2017) 29672–29678.
[28] S. Johnsen, Z. Liu, J.A. Peters, J.-H. Song, S.C. Peter, C.D. Malliakas, N.K. Cho, H. Jin, A.J. Freeman, B.W. Wessels, M.G. Kanatzidis, Chem. Mater. 23 (2011) 3120–3128.
[29] P.L. Wang, Z. Liu, P. Chen, J.A. Peters, G. Tan, J. Im, W. Lin, A.J. Freeman, B. W. Wessels, M.G. Kanatzidis, Adv. Funct. Mater. 25 (2015) 4874–4881.
[30] P. Blaha, K. Schwarz, G.K. Madsen, D. Kvasnicka, J. Luitz, wien2k, An Augmented Plane Wave+ Local Orbitals Program for Calculating Crystal Properties, Vienna University of Technology, Vienna, 2001.
[31] J.P. Perdew, Y. Wang, Phys. Rev. B 45 (1992) 13244–13249.
[32] F. Tran, P. Blaha, Phys. Rev. Lett. 102 (2009), 226401.
[33] D.J. Singh, Phys. Rev. B 82 (20) (2010), 205102.
[34] J. Camargo-Martínez, R. Baquero, Phys. Rev. B 86 (19) (2012), 195106.
[35] F. Tran, P. Blaha, Phys. Rev. Lett. 102 (22) (2009), 226401.
[36] M. Jamal, M. Bilal, I. Ahmad, S. Jalali-Asadabadi, J. Alloys Compd. 735 (2018) 569–579.
[37] G.K.H. Madsen, D.J. Singh, Comput. Phys. Commun. 175 (2006) 67–71.
[38] Bakhtiar Ul Haq, S. AlFaify, R. Ahmed, Samah Al-Qaisi, M.M. Alsardia, I.B. Khadka, Se-Hun Kim, Ceram. Int. 48 1 (2022) 642–647, https://doi.org/10.1016/j.ceramint.2021.09.143.
[39] Samah Al-Qaisi, Muhammad Mushtaq, Jamila S. Alzahrani, Huda Alkhaldi, Z. A. Alrowaili, Habib Rached, Bakhtiar Ul Haq, Q. Mahmood, M.S. Al-Buriahi, Manal Morsi, Micro Nanostruct. 170 (2022), 207397, https://doi.org/10.1016/j.micrna.2022.207397.
[40] S. Al-Qaisi, A.M. Mebed, M. Mushtaq, D.P. Rai, T.A. Alrebdi, R.A. Sheikh, H. Rached, R. Ahmed, M. Faizan, S. Bouzgarrou, M.A. Javed, J. Comput. Chem. 44 (19) (2023) 1690, https://doi.org/10.1002/jcc.27119.
[41] A. Otero-de-la-Roza, V. Luaña, Comput. Phys. Commun. 182 (2011) 1708–1720.
[42] H. Kalpen, W. Honle, M. Somer, U. Schwarz, K. Peters, H.G. von Schnering, R. Blachnik, Z. Anorg, Allg. Chem. 624 (1998) 1137.
[43] G. Chapuis, Ch Gnehm, V. Kramer, Acta Crystallogr. B 28 (1972) 3128.
[44] V. Kramer, Thermochim. Acta 15 (1976) 205.
[45] V. Kramer, Thermochim. Acta 86 (1985) 291.
[46] V. Kramer, Acta Crystallogr. B 36 (1980) 1922.
[47] Yu Grin, U. Wedig, H.G. von Schnering, Angew. Chem, Angew. Chem. Int. Ed. Engl. 34 (1995) 1204 107 (1995) 1318.
[48] H. Kalpen, Y. Grin, H.G. Von Schnering, Z. Anorg. Allg. Chem. 624 (1998) 1611–1616.
[49] F.D. Murnaghan, Proc. Nat. Acad. Sci. USA 30 (1944) 244.
[50] A. Tomas, M.P. Pardo, M. Guittard, M. Guymont, R. Famery, Mater. Res. Bull. 22 (1987) 1549.
[51] T. Ghellab, Z. Charifi, H. Baaziz, Telfah Ahmad, Riad Ababneh, Alsaad Ahmad, Renat Sabirianov, Solid State Commun. 347 (2022), 114731.
[52] R. Hill, Proc. Phys. Soc. 65 (1952) 349.
[53] R. Hill, J. Mech. Phys. Solid. 11 (1963) 357.
[54] W. Voigt, Lehrbuch der Kristallphysik, 1928.
[55] A. Reuss, Z. Angew. Math. Mech. 9 (1929) 49.
[56] S. F Pugh, Lond Edinb, Dublin Philos. Mag. J. Sci. 45 (1954) 823–843.
[57] S.F. Pugh, M. Philo, The London, Edinburgh, and Dublin philosophical magazine and journal of science, Taylor Fr 45 (1954) 823–843.
[58] S. Al-Qaisi, H. Rached, M.A. Ali, et al., Opt. Quant. Electron. 55 (2023) 1015, https://doi.org/10.1007/s11082-023-05282-x.
[59] S. Al-Qaisi, H. Rached, T.A. Alrebdi, S. Bouzgarrou, D. Behera, S.K. Mukherjee, M. Khuili, M. Adam, A.S. Verma, M. Ezzeldien, J. Comput. Chem. 44 (32) (2023) 2442, https://doi.org/10.1002/jcc.27209.
[60] M.E. Eberhart, T.E. Jones, Phys. Rev. 86 (2012), 134106.
[61] O.L. Anderson, J. Phys. Chem. Solid. 24 (1963) 909–917.
[62] P. Ravindran, L. Fast, P.A. Korzhavyl, B. Johansson, J. Wills, O. Eriksson, J. Appl. Phys. 84 (1998) 4891.
[63] D.H. Chung, W.R. Buessem, Proceedings, Plenum Press, 1968.
[64] S. Ranganathan, M. Ostoja-Starzewski, Phys. Rev. Lett. 101 (2008) 55504–55507.
[65] J.F. Nye, Oxford Science Publications, Clarendon Press, 1985.

[66] Q. Li, et al., Angew. Chem., Int. Ed. 56 (2017) 15969–15973.
[67] M. Vigneshwaran, et al., Chem. Mater. 28 (2016) 6436–6440.
[68] K.-H. Hong, J. Kim, L. Debbichi, H. Kim, S.H. Im, J. Phys. Chem. C 121 (2017) 969–974.
[69] Y. Kim, et al., Angew. Chem., Int. Ed. 55 (2016) 9586–9590.
[70] A.J. Lehner, et al., Appl. Phys. Lett. 107 (2015), 131109.
[71] R.E. Brandt, et al., J. Phys. Chem. Lett. 6 (2015) 4297–4302.
[72] U.H. Hamdeh, et al., Chem. Mater. 28 (2016) 6567–6574.
[73] D.R. Penn, Phys. Rev. 128 (1962) 2093–2097.
[74] D. Behera, M. Manzoor, M.W. Iqbal, S. Lakra, S.K. Mukherjee, Comput. Condens. Matter. 32 (2022), e00723.
[75] G. Konstantatos, L. Levina, J. Tang, E.H. Sargent, Nano Lett. 8 (2008) 4002–4006.
[76] L. Cademartiri, et al., Angew. Chem., Int. Ed. 47 (2008) 3814–3817.
[77] M. Bernechea, Y. Cao, G. Konstantatos, J. Mater. Chem. A 3 (2015) 20642–20648.
[78] C. Coughlan, et al., Chem. Rev. 117 (2017) 5865–6109.
[79] S.G. Deshmukh, V. Kheraj, Nanotechnol. Environ. Eng. 2 (2017) 15.
[80] T. Ghellab, H. Baaziz, Z. Charifi, K. Bouferrache, M.A. Saeed, A. Telfah, Mater. Res. Express 6 (2019), 075906.
[81] T. Ghellab, Z. Charifi, H. Baaziz, Ş. Uğur, G. Uğur, F. Soyalp, Phys. Scripta 91 (2016), 045804.
[82] T. Ghellab, Z. Charifi, H. Baaziz, K. Bouferrache, B. Hamad, Int. J. Energy Res. (2019) 1–15.
[83] Z. Souadia, A. Bouhemadou, S. Bin-Omran, R. Khenata, Y. Al-Douri, S. Al-Essa, J. Mol. Graph. Model. 90 (2019) 77–86.
[84] H.J. Goldsmid, R.W. Douglas, J. Appl. Phys. 5 (1954) 386.
[85] T.M. Tritt, Rev. Mater. Res. 41 (2011) 433–448.
[86] P. Ruleovaa, C. Drasar, P. Lostak, C.P. Li, S. Ballikaya, C. Uher, Mater. Chem. Phys. 119 (2010) 2991.
[87] G.A. Slack, Solid State Phys. 34 (1979) 1.
[88] D.T. Morelli, V. Jovovic, J.P. Heremans, Phys. Rev. Lett. 101 (2008), 035901.
[89] M.A. Blanco, E. Francisco, V. Luania, Comput. Phys. Commun. 158 (2004) 57–72.
[90] S.A. Dar, V. Srivastava, U.K. Sakalle, S.A. Khandy, J. Supercond. Nov. Magnetism 31 (2018) 1549–1558.
[91] B. Hamawandi, H. Mansouri, S. Ballikaya, Y. Demirci, M. Orlovská, N. Bolghanabadi, S.A. Sajjadi, M.S. Toprak, Front. Mater. 7 (2020), 569723.
[92] H. Ma, C.-L. Yang, M.-S. Wang, X.-G. Ma, Y.-G. Yi, J. Phys. D Appl. Phys. 52 (2019), 255501.
[93] T. Ghellab, H. Baaziz, Z. Charifi, M. Telfah, A. Alsaad, A. Telfah, R. Hergenroder, R. Sabirianov, Mater. Sci. Semicond. Process. 141 (2022), 106415.
[94] T. Ghellab, H. Baaziz, Z. Charifi, K. Bouferrache, Ş. Uğur, G. Uğurand H. Ünver, Int. J. Mod. Phys. B 33 (2019), 1950234.
[95] H. Latelli, T. Ghellab, Z. Charifi, H. Baaziz, F. Soyalp, Int. J. Mod. Phys. B 35 (7) (2021), 2150100.
[96] A. Telfah, T. Ghellab, H. Baaziz, Z. Charifi, A.M. Alsaad, R. Sabirianov, J. Magn. Magn Mater. 562 (2022), 169822.
[97] Z. Charifi, T. Ghellab, H. Baaziz, F. Soyalp, Int. J. Energy Res. (2022) 1–19.
[98] T. Ghellab, H. Baaziz, Z. Charifi, H. Latelli, Phys. B Condens. Matter 653 (2023), 414678.
[99] H. Mekki, H. Baaziz, Z. Charifi, T. Ghellab, A.E. Genç, Ş. Uğur, G. Uğur, Solid State Commun. 363 (2023), 115103, https://doi.org/10.1016/j.ssc.2023.115103.